JOINT EUROPEAN TORUS JET

JET–R(89)07

H. Salzmann, J. Bundaard, A. Gadd, C. Gower, V. Gusev, K.B. Hansen,
K. Hirsch, P. Nielsen, K. Reed, C. Schrödter and K. Weisberg

The LIDAR Thomson Scattering Diagnostic on JET

The LIDAR Thomson Scattering Diagnostic on JET

H. Salzmann, J. Bundaard, A. Gadd, C. Gower, V. Gusev, K.B. Hansen, K. Hirsch, P. Nielsen, K. Reed, C. Schrödter and K. Weisberg

JET Joint Undertaking, Culham Science Centre, OX14 3DB, Abingdon, UK

[1]*Institute für Plasrraforschung, Universität Stuttgart, 7 Stuttgart-SO, FRG*
[2]*Risø National Laboratory, Roskilde, Denmark*
[3]*Ioffe Physico-Technical Institute, Academy Sciences USSR, Leningrad, USSR*
[4]*Max-Planck-Institut für Quantenoptik, 8046 Garching, FRG*

ABSTRACT.

By combining the time-of-flight or LIDAR principle with a Thomson backscatter diagnostic, spatial profiles of the electron temperature and density can be measured with a single set of detectors for all spatial points. This approach considerably simplifies the collection optics required for measuring a spatial profile. The technique was realised for the first time on the JET tokamak and has been in routine operation since July 1987. A ruby laser (3J pulse energy, 300ps pulse duration, 0.5Hz repetition rate) together with a 700MHz bandwidth detection and registration system yields a spatial resolution of about 12cm. A large filter spectrometer with 6 spectral channels covering the wavelength range 400–800nm gives a dynamic range of the temperature measurements of 0.3-20keV. The stray light problem in the backscatter geometry is overcome by spectral discrimination and effective gating of the MCP photomultipliers. A high rejection ruby notch filter in the spectral channel containing the laser wavelength allows calibration of the vignetting along the line of sight by means of Raman scattering, thus enabling the measurement of density profiles. The low level of plasma background signal due to the short integration time for an individual spatial point yields low statistical errors ($\Delta T_e/T_e \approx 6\%, \Delta n_e/n_e \approx 4\%$ at $T_e = 6\text{keV}$, $n_e = 3\times10^{19}\ \text{m}^{-3}$). Goodness-of-fit tests indicate that the systematic errors are within the same limits . The system is described and examples of measurements are given and compared with the results of other diagnostics.

CONTENTS

1. INTRODUCTION

By combining the LIDAR (Light Detection and Ranging) and Thomson scattering techniques a new method for obtaining electron density and temperature profiles has been applied for the first time on the JET tokamak [1]. The method was proposed in [2] and [3], and during the development of the system for JET several aspects have been described [4-7]. The system is especially well suited for fusion devices that become inaccessible due to activation, since the collection optics required in the vicinity of the device are very simple. Further, this method yields measurements with smaller statistical errors at given laser energy than conventional Thomson scattering systems. This is due to the lower plasma light signal level achieved by the short integration time for each spatial point.
This report is similar to a recent publication [8], but here we have been able to include more details both with respect to technical solutions and analysis procedures.

2. GENERAL DESCRIPTION

2.1 PRINCIPLE OF MEASUREMENT

The spectrum of the backscattered light, generated by a short laser pulse as it traverses the plasma, is recorded as a function of time by a fast detection system. Analysis of the scattered spectrum yields the electron temperature and density in the usual way [9]. However, the position of the laser pulse within the plasma is also known at any instant in this time-of-flight method. Thus, by analysing the spectrum as a function of time, both the electron temperature and density are determined as a function of the space coordinate along the line of sight.

The spatial resolution δL of such an arrangement is given by $\delta L = c(\tau_L + \tau_D)/2$, where c is the speed of light, τ_L is the laser pulse duration and τ_D is the combined response time of the detection system. This relation can be verified easily using the space-time diagram shown in Fig. 1. The two parallel straight lines with positive slope indicate the world lines of the front and back of a laser pulse of duration τ_L travelling forward in space. The two parallel lines with negative slope are the world lines of a pulse of backscattered light which can be resolved by the detection system.

In the LIDAR system described here, the laser pulse duration is 300 ps and the overall bandwidth of the detection and registration system is about 700 MHz. This results in a spatial resolution of approximately 12 cm, a value which is sufficiently small compared with the dimensions of the JET plasma (minor radius ~1.2 m).

2.2 SYSTEM OVERVIEW

The general layout of the system is shown in Fig. 2. The laser and all sensitive components of the detection system are located outside the biological shield around the JET torus hall. The laser beam and the collected scattered light are passed in and out via a labyrinth penetration in the torus hall ceiling. In the torus hall the laser beam is directed towards the torus inner wall by a single dielectric mirror. There is no beam dump as such, the beam is directly incident on one of the carbon tiles covering the torus wall. Before passing the entrance window the beam polarisation is rotated through 90° by a half-wave plate in order to reduce the stray light level in the polarisation plane of the scattered light.

The backscattered light is collected by a folded spherical mirror system through an array of six windows surrounding the laser input window on the JET vessel. Its effective solid angle of collection is $d\Omega = 5.5 \times 10^{-3}$ sr. The collection system is shared with the 90° Thomson scattering system, for which it was constructed [10].

From the labyrinth, the scattered light from the LIDAR system is passed to the spectrometer, where gated MCP photomultipliers detect the power in the different wavelength bands. The fast transient recorders digitize the photomultiplier signals and send the data into CODAS, the JET data acquisition and control system, for analysis.

3. THE LASER

The laser (Fig. 3) consists of an actively mode-locked oscillator, two single pulse selectors in series followed by four stages of amplification. Vacuum spatial filters are inserted between the final three stages to control the transverse mode structure. The main parameters of the laser are summarised in Table I.

Table I

Laser Beam Parameters

Energy (single pulse)	5 J
Energy (0.5Hz rep. rate)	3 J
Wavelength	694.3 nm
Pulse Duration	300 ps
Beam Divergence	250 μr
Diameter	40 mm
Pre-pulse Suppression Level	10^8

The frequency of the 50 MHz acousto-optic modulator, positioned close to the 100% reflectivity cavity mirror, just matches the optical round-trip time of light pulses within the oscillator and mode-locks the cavity oscillations. The RF drive power of the modulator can be varied to control the duration of the individual pulses in the mode-locked train and a further level of pulse width control is afforded by the inclusion of an intra-cavity etalon. Pulses in the range 180 to 600 ps duration can be generated but the oscillator is invariably set to produce 300 ps pulses. This duration is a compromise between the conflicting requirements of achieving good spatial resolution with the diagnostic whilst minimising the risks of damage in the optical components. The energy stability of the output pulse train from the oscillator is improved by partially opening the Q-switch a few micro-seconds early, allowing a short period of pre-lase. Optical triggering of an electro-optic shutter (Single Pulse Selector) allows one of the larger pulses from the oscillator pulse train to be switched through to the amplifier chain for amplification from the millijoule energy level up to 5 J. The second SPS unit is necessary to meet the pre-pulse contrast of about 10^8 required by the diagnostic. This high suppression level is necessary to prevent stray laser light, produced by pre-pulses as they strike the inner torus wall, from swamping the scattered light signal produced by the main laser pulse. Examples of the oscillator pulse train, the switched-out pulse duration and the final output pulse energy when the system is run at 0.5 Hz are given in Fig. 4.

4. THE INPUT OPTICS

The input optics must relay the laser pulse to the scattering volume. The beam cross section through the plasma is approximately constant (~50 mm diam.). The laser is located in the roof laboratory, resulting in a total distance of 50 meters between laser and scattering volume. The penetration through the torus hall ceiling is arranged as a neutron attenuating labyrinth. Because of the labyrinth and the large distances the beam path is convoluted, using five mirrors.

The relay optics consist of two lenses, forming a beam expander with beam expansion of 1.2. Both lenses are positive. The first lens located at the laser output focuses the beam through a pinhole ensuring a beam divergence of < 1 mrad. The second lens of the beam expander is chosen to also image the laser output onto the scattering volume, thus ensuring uniform beam intensity. The section between the beam expander lenses is evacuated to prevent breakdown at the focus. The beam size at all optical components is kept larger than the beam size at the laser output to avoid laser damage.

The input optics also include a He-Ne laser based alignment system to allow the beam path to be remotely aligned to the torus. A coaxial He-Ne laser beam is expanded to 1.5 times the size of the ruby beam. In this surrounding beam are placed four pairs of 5 mm diameter retroreflectors. The retroreflector pairs are located at different positions along the beam path where the laser beam is parallel. The reflections from the corner cubes are imaged back to the laser bench, and their lateral positions with respect to the ruby laser beam are determined by position sensitive Si-photodiodes. Most mirrors in the beam path are motorized.

The laser beam-steering mirror in the equatorial plane of the torus can be used to scan all the windows including the observation windows with the repetitively pulsed laser beam. This will be applied to ablate any absorbing deposits on the inside of the windows which may eventually could impair the measurements (especially if they have spectrally varying absorption).

5. THE COLLECTION OPTICS

For the collection and transmission of the scattered light the same optics are used as for the single point Thomson scattering system which was described in [10]. The main parts of the collection optics are shown in Fig. 5.

The scattered light passes through 6 quartz windows of 0.17 m diameter arranged on a circle of radius 0.19 m around the central laser input window. The windows are located on a pumping port at a major radius of 7.5 m, at a distance of 4.45 m from the plasma centre. Two shutters inside the torus are used to protect the windows against deposits during cleaning discharges and carbonisation.

In order to monitor the window transmission, the plasma is viewed via optical fibres at different wavelengths i) through one of the collection windows and ii), for reference, through the laser input window which stays clean due to laser ablation.

A vertical array of six aluminium coated spherical mirrors (0.3 m diameter, 2.0 m focal length) with a common centre of curvature is located at a major radius of 11.6 m and images the plasma centre onto a small plane mirror which is inclined by 45° and mounted behind the laser beam steering mirror. This Newtonian mirror reflects the scattered light onto a horizontal array of six spherical mirrors positioned underneath. These mirrors image the Newtonian mirror onto a 0.2 m x 0.3 m quartz field lens above the penetration of the 2.3 m thick concrete ceiling. This field lens will also serve as a tritium seal during the D-T phase of JET operations.

Above the ceiling penetration a labyrinth is set up with two plane broadband mirrors. In the tritium phase of

operation this labyrinth will be encased in a concrete shielding block to reduce the neutron flux into the roof laboratory.

After passing an achromatic doublet image relaying lens (Fig. 6) and an aspheric corrector plate which compensates the spherical aberrations caused by the Newtonian telescopic system, a 1:1 image of the plasma centre is formed in the plane of the entrance slit of the spectrometer of the single point Thomson scattering system. This entrance slit consists of a 3.5 mm x 50 mm uncoated area of an aluminium coated, inclined mirror. By this simple geometrical means the beams of collected light of the two scattering systems are separated from each other (see Fig. 9). The reduction of the LIDAR Thomson signal amplitudes caused by the slit is smaller than 7% in the worst case.

The collection optics is characterised by an F-number of F = 8, an étendue of 1 cm^2sr and a transmission T ≈ 15% which is approximately constant over the whole spectral range of 400 - 800 nm.

6. THE SPECTROMETER

The choice of the type of spectrometer is constrained by a number of requirements. Firstly, it must offer a high optical étendue for an incident light beam of circular cross section. This requirement rules out the use of grating and prism spectrometers, but it can be met using interference filter polychromators. Secondly, since the complete radial temperature profile is to be measured with a single instrument, the spectrometer should offer about six spectral channels in order to ensure a dynamic range of about 0.2 - 20keV. A possible solution for this would be a filter polychromator with six passband interference filters put in series in a zig-zag geometry with relay lenses between them, as used on ASDEX [11]. However, in addition, the spectrometer has to cope with the problem that the scattering volume moves along the line of sight of the collection optics during the measurement. Consequently, the intensity distribution in a fixed image plane changes from a small, well-defined image to a larger, blurred spot. This could lead to changes in the spectral transmission due to filter inhomogeneities. This effect has been avoided by placing the filters in the image planes of the collection mirror system. Thus the same area of a filter is used for all scattering volumes.

The solution adopted, which uses interference edge filters instead of bandpass filters meets the given requirements in a rather compact set-up. Its principle is sketched in Fig. 7.

An image is formed of the collection optics which is illuminated homogeneously by the broadband scattered light. Within the depth of focus n short wave pass dielectric edge

filters i = 1...n are placed behind each other but tilted with respect to each other. The edge wavelength of the filter i is chosen to be shorter than that of the preceding filter i-1. Thus n beams of light are reflected from the filter stack into different directions, each beam containing the wavelength range defined by the edge wavelengths of two adjacent filters i and i-1. Since dielectric edge filters are not 100% transmitting in the transmission region a small quantity of this short wavelength light is also present in the reflected beam, thus the complete short wavelength range has also to be suppressed in each spectral channel. This is done by means of absorbing coloured glass edge filters. Thus the transmission $\Gamma(\lambda)$ of the spectral channel k is given by

$$\Gamma(\lambda) = (1 - T_k(\lambda))\, T_{CGF,k}(\lambda) \prod_{i=1,n-1} T_i^2(\lambda), \quad \text{eq. (1)}$$

where $T_i(\lambda)$ is the spectral transmission of the interference edge filter i and $T_{CGF,k}(\lambda)$ is the spectral transmission of the colour glass edge filter in channel k. Multiple reflections within the filter stack do not impair the performance of the spectrometer since they 'walk-off' the reflected main beam paths.

In addition to the spectral channels observed in reflection, a spectral channel which comprises the shortest wavelength range exists in transmission.

All filters consist of hard TiO_2-SiO_2 layers on BK7 substrates with a thickness uniformity of better than ±1% over the aperture of 120 mm. The filters are AR-coated on the rear surface.

The optical transmission losses of the spectrometer can be reduced by avoiding the reflection losses from the back surfaces of the plane filter substrates. This can be accomplished using wedge plates and applying consecutive edge filter coatings i and i+1 to the front and rear side of the wedges. Such filters have been prepared for the spectrometer. While fixed-wavelength combined optical and quartz-monitoring [12] on multiple test-glasses was used for the production of the plane filters, the higher risk of depositing two filters on one wedge plate put even more stringent requirements on the process control. These thin film systems of 23 layers each were deposited on single test-glasses recording spectra of the filter in production after each layer [13]. Refractive indices of the individual layers including dispersion and thicknesses were calculated from these spectra by inverse synthesis [14]. The deposition parameters of the following layers were then optimized numerically in order to make up for deviations from the original design that had occurred so far. Fig. 8 shows the characteristics of the four filters.

In Fig. 9 the complete spectrometer set-up is shown, using the wedge plate configuration in place of the plane substrate filters currently in use.

An additional spectral channel is set up by a fifth edge

filter placed at an angle of 45° in front of the stack, again in an image plane of the collection mirrors. The long wavelength range 650 - 850 nm is taken out of the incident beam of light by this filter while the whole short wavelength range 400 - 650 nm is passed. Design and fabrication of this special edge filter thus appear more difficult than those of the others. Optical monitoring during deposition for instance is carried out at normal incidence where the system's spectral characteristic is quite different from that at the angle of incidence of operation. At this large angle it also becomes distinctly polarization dependent. S-polarization was chosen to obtain sufficient reflection in the stop band with a moderate number of layers (25), which is advantageous for keeping ripples in the pass band small. In order to avoid a still deeper drop in transmission in the shorter wavelength region caused by strong dispersion of TiO_2 near its absorption edge, HfO_2 was used for that filter as high-index material.

As can be seen from Fig. 9, a number of AR-coated lenses between the edge filters are used for image-relaying. Image relaying is used also to image the collection mirrors onto the detectors. Thus once again the same, homogeneously illuminated, area of the photocathode is used throughout the measurement. As a corollary this also ensures that no local saturation of small areas of the proximity focused microchannelplate photomultiplier occurs.

From the design of the edge filter polychromator it is evident that the spectral rejection against stray ruby laser light will vary considerably among the different spectral channels. High rejection ratios are to be expected for spectral channels where the light passes through several edge filters, but for the channels observed in reflection a limit will be set by scattering of light from the first surface of the filter stack. In order to improve the performance of these spectral channels, two small additional edge filters are inserted in front of each of the detectors 2 and 3, and one edge filter in front each of the detectors 4 and 5. Since these channels are spectrally well separated from the laser line, the decreased slope of the (inclined) edge filters due to operation in an F/1.2 converging light beam presents no problems. By illuminating the spectrometer with attenuated ruby laser pulses the stray ruby laser light rejection for the different channels was measured to be 10^7 in channel 2, 10^8 in channel 3 and $>10^8$ in the channnels 4, 5 and 6.

Another approach to suppress spectrally unshifted stray light was chosen for channel 1. Here, a highly doped ruby crystal filter is inserted in front of the detector, a method described by several authors [15-19]. The crystal shows high absorption at the ruby laser line but transmits light with wavelengths near to this line with only small losses. The filter consists of an array of 64 ruby crystal blocks with a doping of up to 2.3% by weight of chromium oxide. The array

has a square cross section and is 15 mm thick. The c-axes of the 64 crystals are aligned to be parallel to each other in the surface of the filter, perpendicular to both the E-vector and the wave-vector of the incident light.Suppression factors of more than 10^6 were measured for individual blocks, the effective overall suppression factor of the assembled array being 10^4. A detailed description of the ruby filter has been published [20].

The spectral "slit" functions (Signal / photon, normalised to maximum) of the six channels are shown in Fig. 10. In these measurements the narrow dip in channel 1, caused by the ruby filter, is not spectrally resolved since a tunable light source with a spectral width of 1.5 nm FWHM was used (see Sec. 9). The predicted insensitivity of the slit functions against changes in the location of the scattering volume was checked by performing measurements with different illumination of the spectrometer, corresponding to different positions of the scattering volume along the line of sight. No changes were found.

Cross-talk between the channels is less than 1% and is negligible considering the SNR-values of the Thomson measurements.

The long term stability of the spectrometer is sufficient for the Thomson backscatter measurements. During the 18 months operational life of the system up to now, several independent calibrations have been carried out and no significant changes in the spectral slit functions have been detected.

7. DETECTORS

The detectors required for the system need to combine a large sensitive area of about 20 mm diameter with a risetime of less than 300 ps and a gain of about 10^5. They also need to be capable of both efficient gating in order to facilitate stray light suppression and of rapid recovery from saturation by intense light pulses. All these requirements are met by the proximity focused ITT F 4128 microchannelplate photomultiplier.

The detectors are gated-on by applying a 130 V pulse to the gap between photocathode and MCP input. A stationary bias voltage of -10 V across this gap results in a closure ratio of $> 10^{13}$ at the ruby laser wavelength, the MCP being kept at full gain all the time [21].

The gating circuitry described in [22] ensures very low interference pick-up on the output signal and constant gain throughout the time of measurement. The low pick-up level of < 10 mV was obtained by using a gating pulse with a smooth leading edge of 7 ns risetime (this time is acceptable due to the long distance between the laser input window - a main

source of stray light - and the outer plasma edge). The constancy of the gain during the measurement is demonstrated in Fig. 11b. The detector parameters are listed in Table II.

Table II

Detector Parameters

Type:	ITT F 4128 proximity focused MCP photomultiplier
Active Area:	20 mm dia.
Gain:	10^5
Risetime:	< 300 ps
Spectral Sensitivity:	MA1 (≈ S20)
Shutter Ratio:	> 10^{13} @ 694 nm
	> 10^8 @ 400 nm
Recovery Time:	~ 50 ms
Operating Voltages:	
Photocathode - MCP	
Bias	- 10 V
Gate Pulse	+ 130 V
MCP	≤ 1800 V
MCP - Anode	300 V

8. REGISTRATION AND DIGITISING

The signals of the photomultipliers are recorded by six TEKTRONIX 7912AD transient digitisers, upgraded by the manufacturer to 800 MHz bandwidth when used with high sensitivity 7A29 pre-amplifier plug-ins. The use of these pre-amplifiers to register the scattering signals in the 100 mV range is complicated by the fact that the detectors deliver pulses of about 300 V amplitude and a risetime of < 300 ps at the end of each measurement when the laser pulse hits the inner torus wall. Since the pre-amplifiers would get destroyed by these transients, the pulses have to be clamped to a safe voltage level (≈ 40 V) without degrading the bandwidth of the detection system. By using at the transient recorder input a fast, biased Schottky diode to clip the forward travelling (negative) pulse to - 40 V and an attenuator at the photomultiplier output to reduce the (positive) reflections, pulses of both signs are kept to a safe level for the pre-amplifier. Details of this solution are described in [22].

The transient digitisers are read out sequentially by

the JET CODAS data acquisition system in the two second interval between consecutive laser pulses.

9. CALIBRATION

To enable the evaluation of the scattering signals a number of calibrations have been performed in addition to those common for Thomson scattering experiments.

a) Sweep Linearity of the Digitisers

A 100 MHz crystal oscillator with an accuracy of better than 5×10^{-5} is used to recalibrate regularly the time bases of the TEK transient digitisers. Changes in the sweep velocity of less than 0.5 % have been measured over a time interval of 1.5 years.

b) Time Correlation of the Signals

On each signal trace a time mark is produced by feeding light from the laser pulse to the detectors via a low dispersion, high bandwidth optical fibre. These time marks serve to correlate the signals in time.

In order to facilitate the conversion of the marker times to the corresponding values of the major radius, a number of different measurements were performed.

First, the timing of the marker pulses relative to the times of arrival of the light pulses from the inner wall was measured for each channel by attenuating these light pulses to the level of linearity of the detectors. These measurements showed that the light pulse observed when the laser pulse hits the inner wall is not only composed of stray light. A small plasma is created which emits light over the whole spectral range of observation. This was verified by introducing coloured glass (long wave pass) edge filters in front of the detectors which transmit the ruby laser wavelength but absorb in the spectral range of the corresponding channel. The plasma radiation dominates the signals in the short wavelength channels whereas in channels 1 and 2 the observed signals are mainly due to laser stray light. Thus, in channels 1 and 2 the pulse shape of the (suitably attenuated) signals from the inner wall equals that of the time markers, whereas in the short wavelength channels the signals display an only slightly longer decay time. For the determination of the time interval to the marker pulses the pulse maxima are used.

Second, the spectrometer was illuminated with a spectrally broadband subnanosecond light pulse. This light pulse was created using the high-frequency electro-optical Kerr effect for switching a short light pulse out of a beam of light from a cw light source [23,24]. For the purpose the

cw light beam and the ruby laser beam were intersected at an angle of 90° in a dye cell containing CS_2 which was placed between crossed polarisers for the cw beam (Fig. 12). The ruby laser pulse was delayed by an appropriate time to produce a light pulse incident onto the detectors about 10 ns after the time marks.

In Table III the results from the CS_2 technique are compared with those used initially and obtained from attenuated inner wall signals. These values were supported by calculations of the expected time differences between channels based on measurements of the different optical path lengths (corrected for refractive index effects). As can be seen, with the exception of channel no. 2, the data agree to better than 100 ps, a value which corresponds to the sampling rate of the digitising system. The channel 2 discrepancy is not yet understood, but is generally of minor importance for the plasma profile measurements.

Table III

Relative Timing of Channels

CH no.	δt (inner wall)	δt (CS_2)
1	0 ps	0 ps (reference)
2	-250	-460
3	-200	-290
4	-10	+90
5	+540	+490
6	+50	+70

The absolute timing of the signals required for measuring the position of the plasma with respect to the cold torus vessel was determined from the time of the stray light pulse from the inner wall measured in the spectral channel 1. An additional check was carried out by placing a glass scatter-plate inside the torus at the position where the laser beam paths of the LIDAR system (horizontal) and of the Single Point Scattering system (vertical) cross each other. This radius was surveyed to be 3.045 m (cold vessel).

An indication for the spatial resolution obtained by these measurements is given by the observation that the signals from the inner wall are shifted with respect to the time marks by about 100ps, corresponding to 1.5 cm, when the vessel is heated up to 250° C.

c) Spectral Slit Function

The spectral "slit" functions of the six spectral channels have been measured by illuminating the spectrometer with a beam of light simulating the characteristics of the collected light beam such as cross section, divergence and

polarisation. A KRATOS 1 kW high pressure Xe arc lamp together with a KRATOS GM 252 F/3.6, f = 0.25 m grating monochromator is used as tunable light source. The power of the output beam after passing a diffuser and a sheet polariser is monitored by a UDT Model 61AC power meter.

d) Relative Sensitivity of the Spectral Channels

The relative sensitivity of the spectral channels has been measured by illuminating the collection optics with a black body light source of calibrated colour temperature: a diffuse reflector painted with a titanium oxide pigment supplied by the NPL Teddington, UK, is placed in front of the torus windows and is illuminated by an OPTRONIC 1 kW spectral irradiance standard lamp Model 100A, powered from a current stabilised supply. Since the overall sensitivity of the collection, dispersion and detection system has to be calibrated for the direction of polarization of the laser beam inside the torus, measurements have to be done with a (large size sheet) polarizer in the beam of collected light. Thus, in addition to the quantities $T_{\parallel}$ and $T_{\perp}$, the combined transmission of the collection and dispersion system parallel and normal to the polarization of the scattered light, another quantity has to be measured (the spectrally dependent maximum transmission of the polarizer). Consequently, three different measurements are used to determine the quantity $S*T_{\parallel}$ for each channel, where S is the detector sensitivity. These are transmission measurements with
i) one sheet polariser parallel, ii) one polariser crossed to the polarisation of the scattered light and iii) without any polariser.

e) Vignetting

As can be seen from Figs. 5 and 6, the solid angle of collection varies strongly along the line of sight, the collection mirrors being far away from the window array. This vignetting has to be determined in order to evaluate density profiles.

Raman scattering from air at atmospheric pressure was used to determine the relative variation of the solid angle of collection as a function of the position of the scattering volume (Fig. 11a)[20]. The spectral width of the absorption maximum of the ruby rejection filter is small enough to pass approx. 90% of the Raman scattered light. The required absolute calibration for density measurements was then achieved by normalising the line integral of the electron density as measured by Thomson scattering to the corresponding line integral measurements by the FIR interferometer in a series of reference discharges.

A further test was carried out in order to establish that the vignetting along the line of sight is the same for

all spectral channels. An incandescent light source with a diffuser and a stop (equal in size to the cross section of the laser beam) in front of it was moved along the line of sight inside the torus vessel and measurements were taken at 47 spatial points. The ratios of the signals from the different channels were found to be constant over the whole diameter of the vessel.

f) Relative Gain of the Detectors

Since different supply voltages of the detectors are used to cope with the different plasma scenarios (pellet injection, RF heating etc.), the gain variation of the MCP photomultipliers with voltage was calibrated (Fig. 13).

g) Single Photoelectron Signal

The detected signal per single photoelectron (mV*nsec) is required for proper weighting of the channels in the fitting procedure. The charge measured per photoelectron may be determined from the manufacturers specifications. However, any excess noise also contributes to the channel noise. We assume that excess noise can be treated in the same way as photoelectron noise (Poisson statistics). To determine the effective noise we illuminate the photomultipliers with a DC light source. The signal levels (no. of pixels) of several thousand time slots are plotted in a histogram and a shifted Gaussian is fitted to it (Fig. 14). The equivalent photoelectron signal is determined by assuming the mean value (shift of the Gaussian) to be equal to a number N of photoelectrons and the halfwidth at the 1/e point to $\sqrt{N}$.

10. DATA PROCESSING

Electron temperature and density are found through a non-linear least squares fit every five centimeters through the plasma. The time corresponding to a given scattering position is determined for each signal as the appropriate time relative to the synchronization pulse described above.

Fig. 15 shows a flow-chart of the data evaluation procedure.

In the LIDAR geometry the scattering angle does not change significantly either with scattering position or within the solid angle of collection. This allows variations of the spectral density function with scattering position and angle to be ignored. At the large scattering angle and with the high temperatures found in JET it is necessary to use the complete relativistic spectrum. To calculate the spectrum at a given temperature involves a numerical integration of a complex function [10]. To speed up the fitting procedure the

spectral density function convoluted with the slitfunctions of the six channels is tabulated for each channel i. The expected signal f_i at every 100 eV for a density of $1x10^{19}$ m^{-3}, unit solid angle and a laser energy of 1 J is listed (Fig. 15a). This table is used as a look-up table by the fitting programme.

In a second step the data are prepared for the fitting procedure by applying the existing calibration values to the measured signals. This yields the scattered signal y_i in no. of photons per channel (at unit solid angle) and its standard deviation σ_i (Fig. 15a). The value of y_i is determined as the difference between the instantaneous light level and the average plasma light level, whereas the standard deviation σ_i is derived from the total light level.

In order to determine the electron temperature and density the absolute minimum of Chi^2 in the T_e,n_e plane is located. Chi^2 is defined by:

$$Chi^2 = \Sigma_{i=1,n} (y_i - f_i*n_e')^2/\sigma_i^2 \qquad \text{eq. (2)}$$

where y_i is the measured value, f_i is the theoretical value, σ_i is the standard deviation and n is the number of spectral channels [25]. n_e' is the density (in units of $1*10^{19}$ m^{-3}) corresponding to the parameters of the look-up table, that is 1 J of laser energy and unit solid angle.

Fig. 16 illustrates schematically how the minimum value of Chi^2 is found in the T_e-n_e' plane. At a number of temperatures the value of n_e' at which Chi^2 is a minimum can be determined by equating the partial derivative of Chi^2 with respect to n_e' to zero. This yields:

$$n_e' = 1*10^{19} * \Sigma_i \{f_i*y_i/\sigma_i^2\} / \Sigma_i \{y_i^2/\sigma_i^2\} \qquad \text{eq. (3)}$$

The value of Chi^2 at this T_e/n_e' point is then calculated from eq. (2).

As an example, Fig. 17 shows Chi^2 vs. T_e along the 'search trajectory' (bold solid line in Fig. 16) for the plasma centre of an RF heated discharge. In order to speed up data processing, the fitted temperature is found by locating the minimum of the parabola on which the three smallest Chi^2 values lie (see Fig. 17, insert). The upper and lower limits of temperature are the temperature values which increase Chi^2 by one over its minimum value [25]. The standard deviation of n_e' is determined at the fitted temperature value again using linear regression.

The absolute values of n_e and its upper and lower bounds are then determined using the calibrated variation of the solid angle of observation along the line of sight and the measured actual laser energy (Fig.15b).

The spatial resolution of the system is limited by the finite pulse width of the laser and the response time of the detection system. The detected signal can be described as the convolution of the scattered signal from different scattering volumes with the response function of the complete system:

$$S_m(t) = \int_{-\infty}^{+\infty} S_s(t-\tau)*G(\tau)\, d\tau \qquad \text{eq. (4)}$$

where S_m is the measured signal, S_s is the scattered signal we would obtain with an infinitely short laser pulse and a detection system with an equally short risetime, and $G(\tau)$ is the total response function of our real system (Green's function of the system). The response function as used here is the signal we get when scattering from a point source in space $\{S(x) = \delta(x-x_s)\}$. The marker pulse is generated by shining a small fraction of the laser light onto the photocathode. This being equivalent to scattering from a point source, the marker pulse is our measured response function.

The procedure used to solve the integral equation (4) consists of a trial and error approach. In the first step the measured signal $S_m(t)$ is used as an approximation for $S_s(t)$ and the zero order correction term is calculated as follows

$$corr_0(t) = S_m(t) - \int_{-\infty}^{+\infty} S_m(t-\tau)*G(\tau)\, d\tau \qquad \text{eq. (5).}$$

As second approximation $S_s(t) = S_m(t) + corr_0(t)$ is used to derive a new correction term. This method converges rapidly and in practice we observe no further improvement after five iterations. The existence of a finite residual difference term $corr_n(t)$ is thought to be due to noise on the original signal. The observed improvement in spatial resolution obtained by applying the above procedure is about 30%.

Fig. 18 illustrates the typical improvement in a single channel signal in a measurement showing a large gradient at the plasma edge. For comparison we have also illustrated the bandwidth enhancement that can be obtained by a commercially available maximum entropy software package [26] using the same response function. We note that the two methods give virtually the same result. As the simple approach described above is considerably faster this routine is being used routinely to improve the spatial resolution from typically 12 cm to 9 cm.

11. RESULTS

Examples of the raw photomultiplier signals from the different spectral channels are shown in Fig. 19. Note the small level of plasma light relative to the Thomson scattering signals. This is due to the short integration time of 800 ps. The automated analysis procedure locates the timemarkers, subtracts baseline and plasma light levels, applies calibration factors and then fits T_e and n_e values by the method described above to 50 time slices across the 6 spectral channels.

Currently up to 9 profile pairs (n_e and T_e) are obtained at 2 s intervals throughout each JET discharge and a data base containing more than 40,000 profiles has been compiled to date. Fig. 20 shows an example where the differences in profile behaviour during the Ohmic, ICRF, and Pellet Injection phases of a single JET pulse are clearly evident from the LIDAR system data. Normally, major radial points from the outer plasma edge to within 25 cm of the inner wall of the JET torus are accessible. Stray light generated by the leading edge of the laser pulse as it strikes the inner wall prevents measurement in this region. (There is insufficient depth for a beam dump).

Electron temperature profiles from the LIDAR system have been compared with the partial profiles from the standard JET ECE system [27] and Fig. 21a shows an example. The agreement between these independently calibrated diagnostics at 2.8 T central toroidal field is seen to be within the experimental error bounds over the whole profile for both systems. In addition to single profile comparison, the central regions of a large number of T_e profiles from both ECE and LIDAR have been averaged and compared. Fig. 22 shows T_e(LIDAR) vs. T_e(ECE) over the full range of measured temperatures during the last six months of operation in 1988. The slope of the linear regression line gives the systematic difference between the two diagnostics as $T_e(\text{LIDAR}) = 0.85\ T_e(\text{ECE})$, which again is within the calibration accuracy quoted for both diagnostics. Fig. 23 shows the same data plotted against pulse number and demonstrates the long term stability of both systems.

The absolute scale on the electron density profiles from the LIDAR diagnostic alone has an uncertainty of about ± 20%, which in part is due to uncertainties in the available Raman scattering cross section data for N_2 and O_2 (about ± 10%). However, the relative density errors (see, for example, the error bars in Fig. 21b) are smaller and are dominated by the effects of photoelectron statistics. Thus, the final value of the absolute scale has been fixed by comparing line integrals derived from the LIDAR data, using magnetic flux surface information, with the data from the JET multi-channel FIR interferometer [28]. Fig. 25 shows the ratio of the line integrated densities computed from the LIDAR profiles

(assuming density constancy on flux surfaces given by IDC2 PPF's) to those measured directly by the FIR system throughout a particular discharge. Generally, agreement to this level is obtained over a period of several weeks of plasma operation without renormalisation of the LIDAR data. This time span indicates the characteristic time for the build-up of deposits on the torus windows.

The detailed shape of the profile revealed by the LIDAR results has increased the confidence in the reality of the structure observed in the profile data from the interferometer when higher order polynomials are used in the inversion procedure. Fig. 21b demonstrates that agreement within the experimental uncertainties is obtained even though the profile shape varies throughout the discharge. The agreement in the density profiles is not obtained when very dynamic events are occurring e.g. during pellet injection, disruptions or the collapse phase of monster sawteeth. However, the indications of hollowness in the density profiles derived from the interferometer results during pellet injection experiments have been confirmed and are clearly resolved in the LIDAR profiles, for example Fig. 21c.

In the analysis of the raw data there remained some residual doubt over the precision achieved in defining the relative timing of the signals from the different channels. Confirmation was afforded by some pellet injection experiments which produced very peaked density profiles. Fig. 25a is an example of the signals obtained on such a pulse and from an examination of the peaks of the signals it is clear that the inter channel timing has been set up to an accuracy of ± 100 ps (± 1.5cm). Fig. 25b shows the corresponding signals for an RF heated discharge. Here the peaks of the signals from the spectral channels far away from the laser wavelength coincide with the dips in signals from the nearby channels.

The Chi^2 goodness-of-fit test can be used to reveal whether the assumptions - the spectral density function given by theory, and the calibration data, measured experimentally - are consistent with the results of the Thomson scattering measurements. The sensitivity of this procedure is demonstrated by a test which was performed in order to investigate the effect on the electron temperature fit of the colour temperature of the standard lamp used. The results of the calibration measurements were processed assuming colour temperatures deviating by ± 100 K and ± 300 K from the specified value (2973 K). An identical set of Thomson scattering signals obtained from 30 monster sawtooth discharges was then evaluated with the five different calibration data sets. Fig. 26 shows the averaged normalised Chi^2 values obtained in different temperature ranges. A distinct minimum of Chi^2 at the specified colour temperature is observed, confirming it to be the correct one. Inferring a systematic error of the colour temperature of 50 K from this

test, the comparison of temperature profiles evaluated with the calibrations corresponding to 2973 K and 2973 ± 50 K shows that the related systematic errors of the electron temperature are less than the statistical errors due to photoelectron noise. This is demonstrated in Fig. 27, where trace a) shows the electron temperature profile with error bars evaluated for a colour temperature of 2973 K, while the traces b) and c) show the fits for assumed colour temperatures of ± 50 K for the same raw data. The traces b) and c) are within the statistical error bars of profile a).

12. OUTLOOK

Since state of the art techniques are used, no significant improvements in terms of spatial resolution and statistical errors are expected to be possible for a full radial profile LIDAR system in the near future. However, a major improvement is possible with respect to the repetition rate of the measurements, using a type of laser capable of higher repetition rates than ruby, e.g. an Alexandrite laser. With respect to better spatial resolution for a limited spatial chord length, required for plasma edge diagnostics for example, a system on the LIDAR basis seems feasible using streak camera detection techniques [3] and shorter laser pulse lengths. Both systems are under construction at JET.
The main LIDAR system will be upgraded to a repetition rate of 10 Hz. This upgrade implies:

1. Installation of a 10 Hz/2 J subnanosecond Alexandrite laser operating at 760 nm.
2. Replacement of the aluminised mirrors of the collection and transmission optics by a set of broadband dielectric mirrors. This will improve the transmission of the optical system by a factor >2, compensating for the lower energy of the Alexandrite laser (compared with that of the present system).
3. Addition of a spectral channel to the spectrometer, covering the wavelength range 720-800 nm. For good sensitivity this channel will use a gated MCP photomultiplier with a semi-transparent GaAs photocathode.
4. Upgrade of the TEK 7912 AD transient digitisers to ensure reliable operation at 10 Hz repetition rate.
5. Parallel data readout from the transient digitisers and data compression to cope with the large data rate.

The existing ruby laser will be used for setting up an edge diagnostic with good spatial resolution (≈ 3 cm). For this purpose it will be operated at a pulse duration of about 200 ps and a streak camera will be used as detection system. The laser will continue to serve as the back-up system for the Alexandrite laser and it is planned that it can be brought into this operational mode at short notice by simply rotating its plane of polarisation.

In our experience the described JET LIDAR system works reliably. Maintenace on a regular basis (about 2-3 months intervals) is required for the laser (to the same extend as is to be expected for lasers used in classical Thomson scattering diagnostics), whereas the complete detection and registration system proved to be very stable. As with all Thomson scattering diagnostics the formation of absorbing deposits on the inside of the torus windows causes calibration problems, but we have found a way to measure their effects which requires neither an opposite window on the torus nor internal mirrors nor radiating heated filaments. Typical time intervals over which deposits build up, requiring recalibration but no cleaning, are of the order of 3-5 months. With respect to longer operating periods without access to the windows, a method of cleaning using laser ablation techniques is planned whereby the laser beam is scanned across the observation windows.

To summarize, the quality of the results obtained with the diagnostic system, its proven reliability and the good compatibility with the requirements of remotely controlled operation render the LIDAR system well suited for large plasma devices.

ACKNOWLEDGEMENTS

During the six years it took from the idea to the working diagnostic numerous people helped us. We wish to thank all of them, especially Dr. G. Brederlow and Dr. K. Witte, MPI f. Quantenoptik, Garching, for the iodine laser investigations during the development phase; Dr. H. Röhr, MPI f. Plasmaphysik, Garching for his advice and encouragement; Dr. P. Stott, JET, for his encouragement and for proposing the shared use of existing optics on JET, which made the diagnostic feasible; Dr. C. Ireland and his team from JK Products Division of Lumonics, Rugby, for providing us with the rugged and reliable ruby laser system; Mr. C. Bjerring and the mechanical engineering group, Risø National Laboratory, Roskilde, for the construction of the optical input and collection system; Mr. B. Bitzenberger from the Institut f. Plasmaforschung, Universität Stuttgart for the mechanical design of the spectrometer; Dr. M. Gadeberg, JET, for his collaboration during the conceptual phase of the project; Dr. A. Costley and the ECE team of JET for their help in starting the project; Dr. H. Murmann from the MPI f. Plasmaphysik for joining us during the exciting nights and days when the diagnostic was assembled and tried for the first time; Dr. P. Carolan, Culham Laboratory for cross-checking our deconvolution method with the MEM software and Mr. B. Brown, JET for his constant assistance with all our numerous technical problems.

REFERENCES

[1] H. Salzmann, K. Hirsch, P. Nielsen, C. Gowers, A. Gadd, M. Gadeberg, H. Murmann, C. Schrödter, Nucl. Fusion 27, 1925 (1987).

[2] R. Kristal, in "Diagnostics for Fusion Experiments", Proc. Course Varenna 1978, Int. School of Plasma Physics, Report EUR 6123, p. 617, Pergamon Press (1979).

[3] H. Salzmann, K. Hirsch, Rev. Sci. Instrum. 55, 457 (1984).

[4] G. Brederlow, J. E. Gruber, K. Hirsch, H. Röhr, H. Salzmann, K. J. Witte, MPI f. Plasmaphysik, Int. Report IPP-1/299, (1984).

[5] K. Hirsch, H. Salzmann, Inst. f. Plasmaforschung, Univ. Stuttgart, Int. Report IPF-85-1, (1985).

[6] H. Salzmann, K. Hirsch, J. E. Gruber, H. Röhr, G. Brederlow, K. J. Witte, Rev. Sci. Instrum. 56, 1030 (1985).

[7] C. Gowers, M. Gadeberg, K. Hirsch, P. Nielsen, H. Salzmann, C. Schrödter, B. Brown, A. Costley, B. Edwards, D. Rand,
in "Basic and Advanced Diagnostic Techniques for Fusion Plasmas", Proc. Course Varenna 1986, Int. School of Plasma Physics, Report EUR 10797 EN, p. 555 (1986).

[8] H. Salzmann, J. Bundgaard, A. Gadd, C. Gowers, K. B. Hansen, K. Hirsch, P. Nielsen, K. Reed, C. Schrödter, K. Weisberg, Rev. Sci. Instrum. 59, 1451 (1988).

[9] J. Sheffield, "Plasma Scattering of Electromagnetic Radiation", John Wiley, New York, (1963).

[10] P. Nielsen, in "Diagnostics for Fusion Reactor Conditions", Proc. Course Varenna 1982, Int. School of Plasma Physics, Report EUR 8351-1EN, p. 225 (1982).

[11] H. Röhr, K.-H. Steuer, G. Schramm, K. Hirsch, H. Salzmann, Nucl. Fusion 22, 1099 (1982).

[12] C. Schrödter, Proc. SPIE 652, 15 (1986).

[13] B. Vidal, H. Pelletier, Appl. Optics 18, 3857 (1979).

[14] C. Schrödter, to be published.

[15] H. Röhr, Kerntechnik 16, 301 (1974) and MPI f. Plasmaphysik, Int. Report IPP 1/57 (1976).

[16] D. H. McNeill, Appl. Optics 15, 573 (1976).

[17] J. A. Cobble, Rev. Sci. Instrum. 56, 1018 (1985).

[18] C. E. Thomas,Jr., E. A. Lazarus, R. R. Kindsfather, S. Painter, P. Hays, M. Murakami, Rev. Sci. Instrum. 57, 1819 (1986).

[19] F. Flora, L. Giudicotti, Istituto Gas Ionizzati, Padova, Int. Report IGI 87/01 (1987).

[20] C. Gowers, K. Hirsch, P. Nielsen, H. Salzmann, Appl. Optics 27. 3625 (1988).

[21] K. Hirsch, M. Köchel, H. Salzmann, Rev. Sci. Instrum. 58, 2339 (1987).

[22] J. Bundgaard, K. B. Hansen, K.-V. Weisberg, Risø

National Lab., Int. Report Risø-M-2699 (1988).
[23] M. A. Duguay, A. T. Mattick, Appl. Optics 10, 2162 (1971).
[24] M. A. Duguay, "Progress in Optics", Vol. XIV, p. 161-193, Ed. E. Wolf, North-Holland Publ. Comp., Amsterdam (1977).
[25] P. R. Bevington, "Data Reduction and Error Analysis for the Physical Sciences", McGraw-Hill, New York, (1969).
[26] Maximum Entropy Deconvolution Package; Maximum Entropy Data Consultants Ltd. Cambridge.
[27] D. V. Bartlett, D. C. Campbell, A. E. Costley, S. Kissel, N. Lopez-Cardozo, C. Gowers, S. Nowak, Th. Oyevaar, N. A. Salmon, B. Tubbing, "Overview of JET ECE Measurements", Proc. of the 6th Joint Workshop on ECE and ECRH, Oxford, Int. Rep. CLM-ECR(1987).
[28] G. Braithwaite, A. Bulliard, J.-L. Bruneau, C. J. Hancock, G. Magyar, J. O'Rourke, A. Nguyen, B. Siri, D. Véron, C. Gowers, A. Hubbard, Int. Rep. JET IR(85)08 (1985).

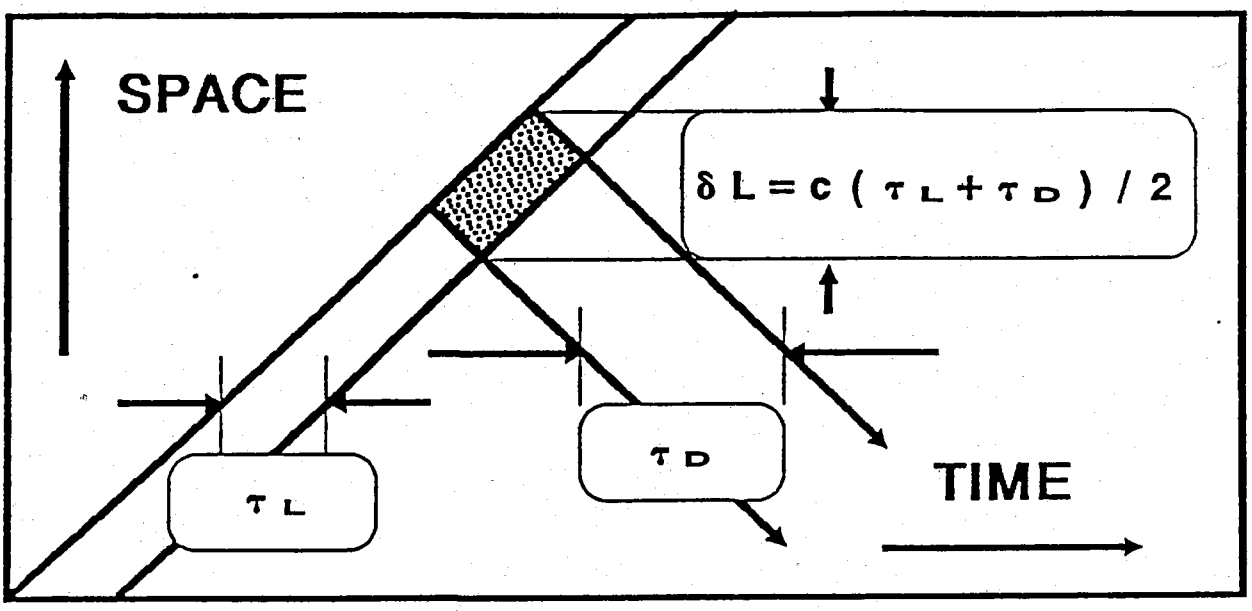

Fig. 1: Space-time diagram of a LIDAR scattering arrangement. τ_L is the laser pulse duration, τ_D is the effective response time of the detection system.

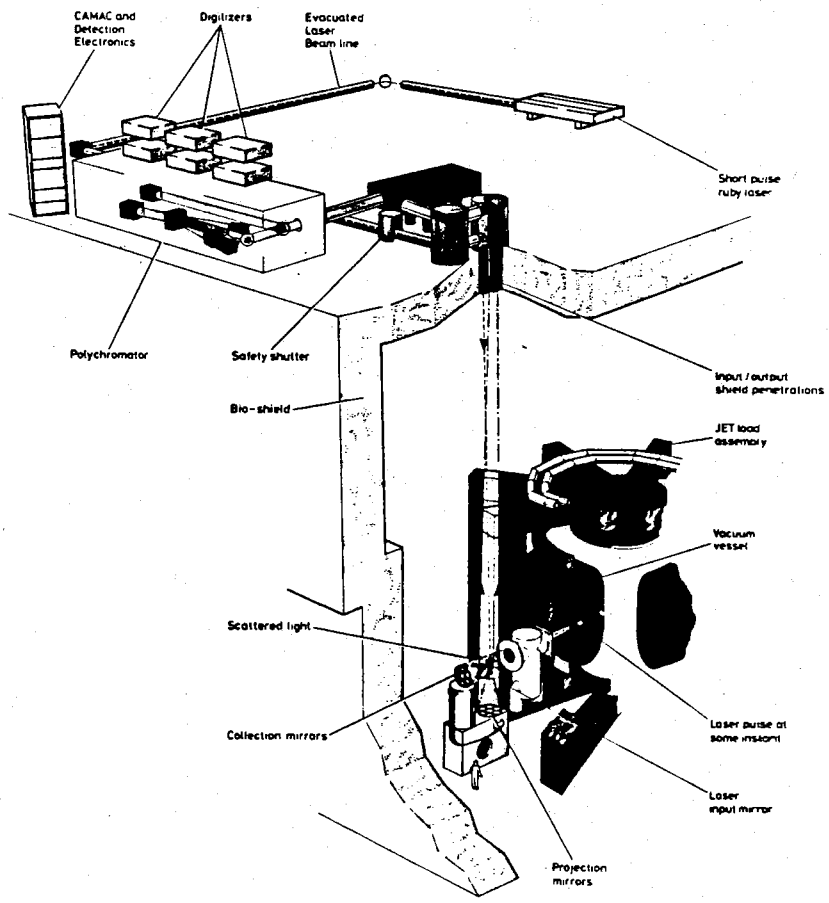

Fig. 2: Lay-out of the scattering system.

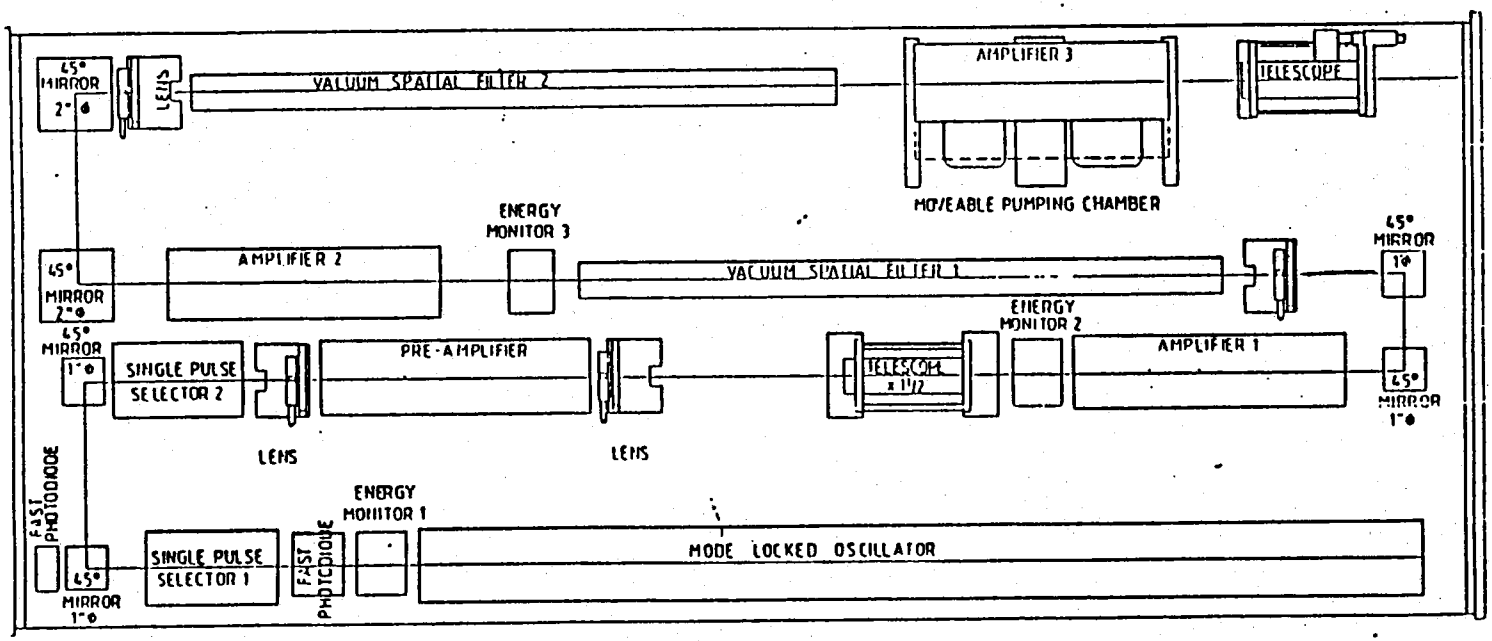

Fig. 3: The ruby laser.

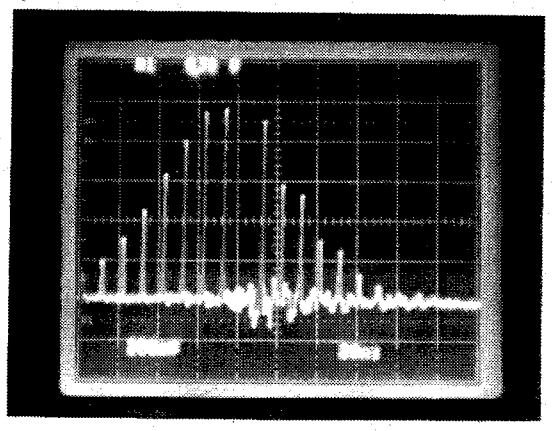

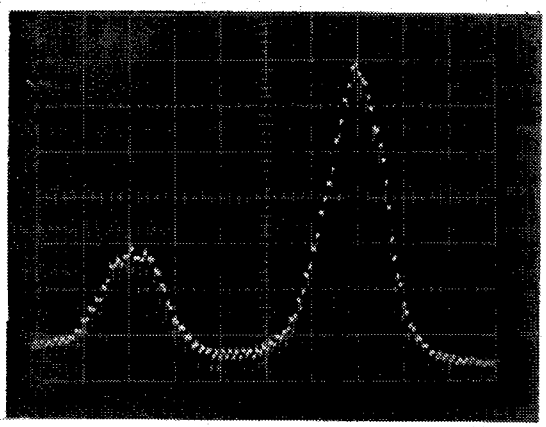

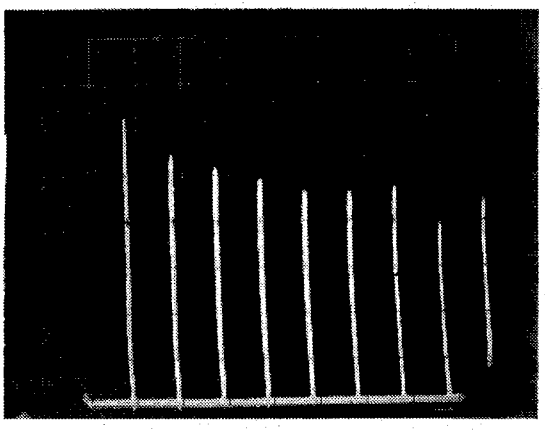

Fig. 4: Laser performance:

a) Oscillator output pulse train monitored by photodiode (risetime ≈ 1 ns) and a 350 MHz oscilloscope. "Missing" pulse has been switched into the amplifier path. Time base: 20 ns / Div.

b) Streak camera record of single pulse and its reflection after a known optical delay (to give time base calibration). Time base: 200 ps / Div.

c) Laser output energy per pulse at 0.5 Hz repetition rate. Vertical sensitivity: 0.4 J / Div. Time base: 2 s / Div.

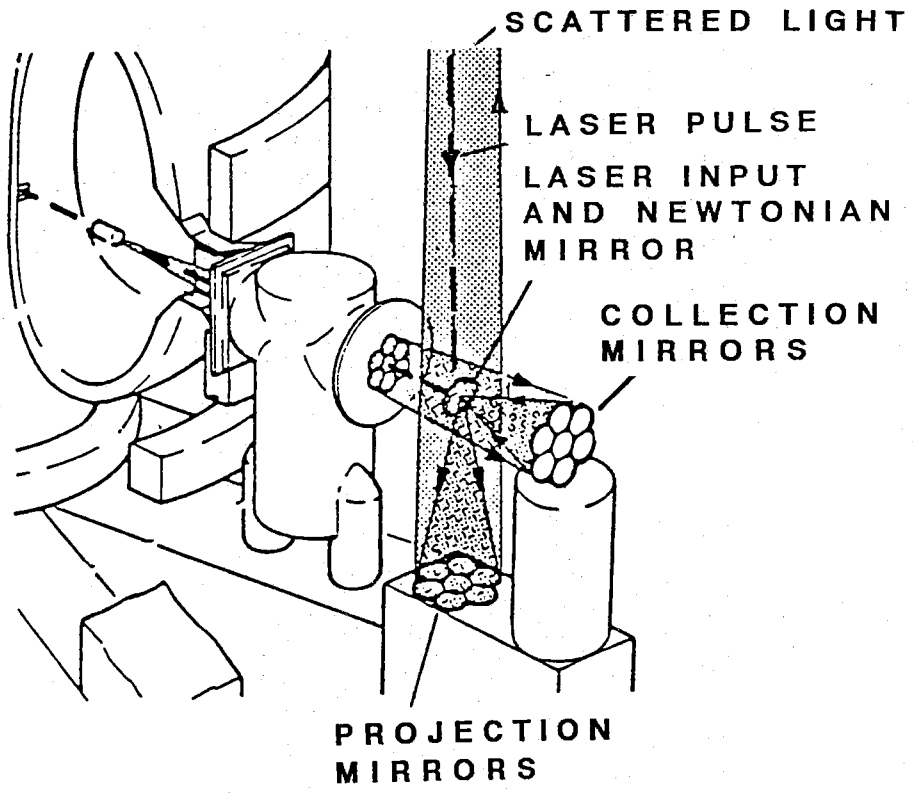

Fig. 5: Schematic of input and collection optics on JET.

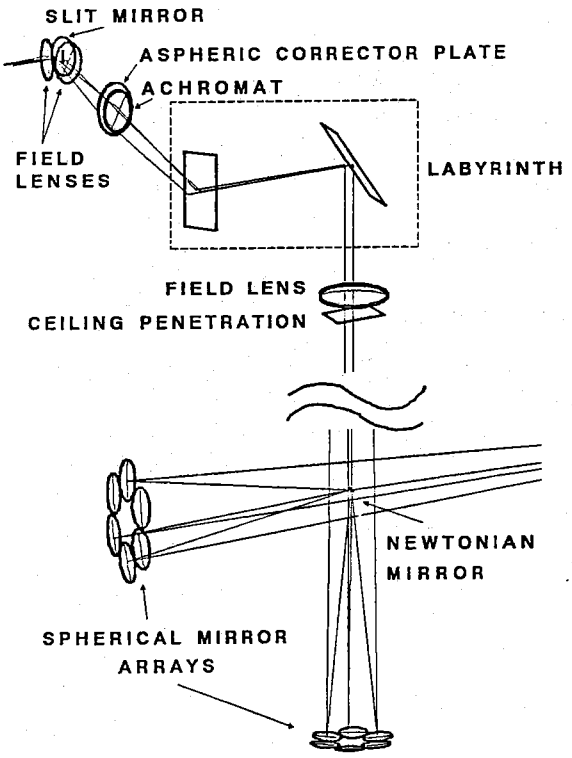

Fig. 6: Collection optics.

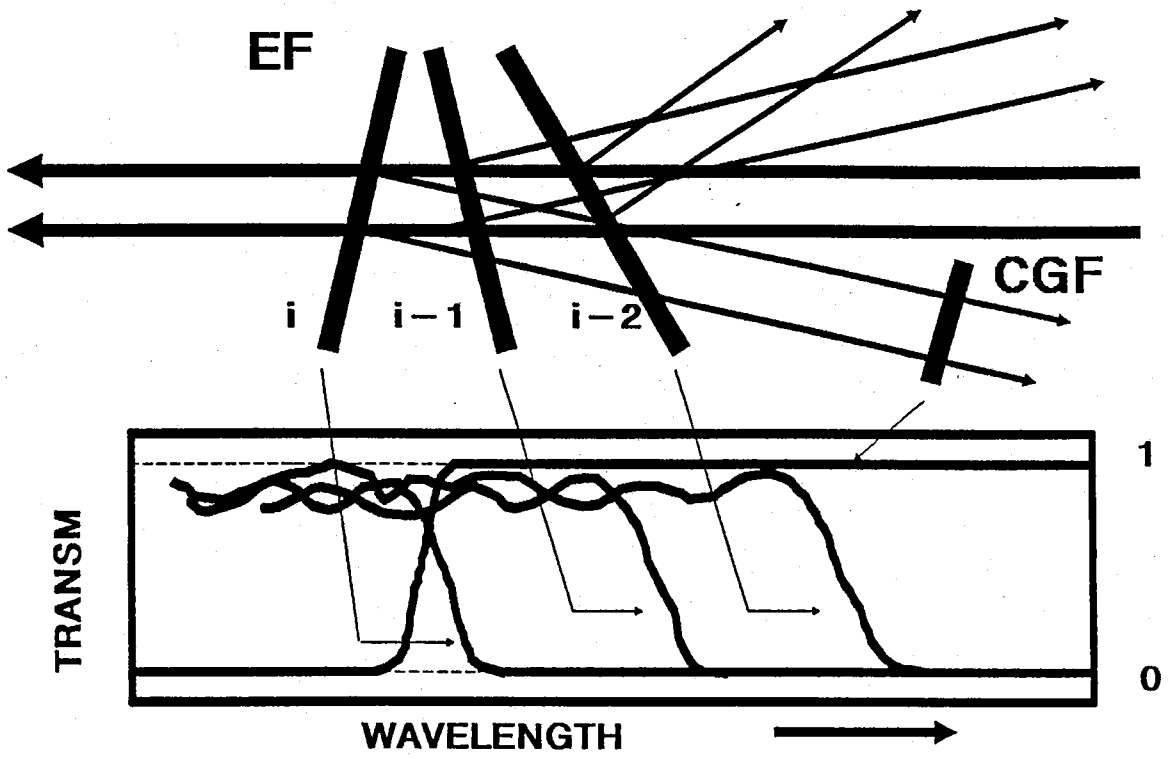

Fig. 7: Principle of the edge filter spectrometer.

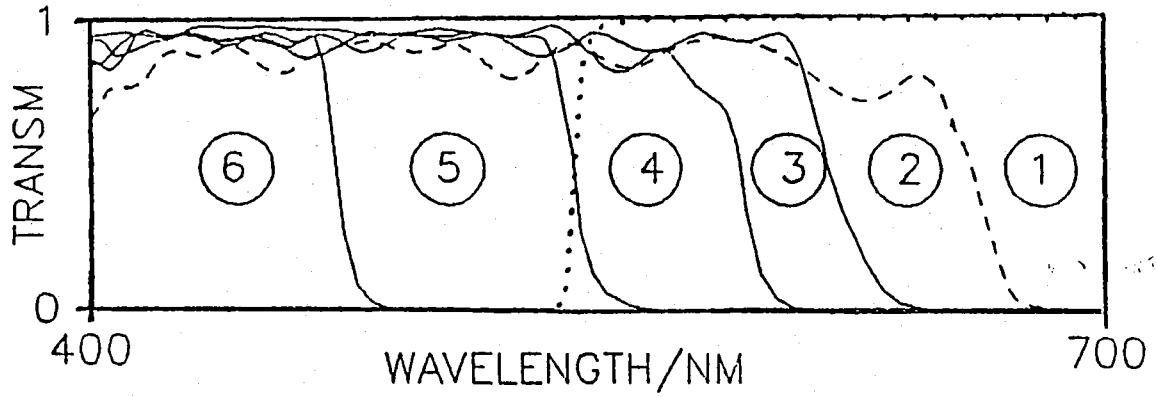

Fig. 8: Spectral characteristics of the wedged plate filters. Broken line: transmission of the 45° edge filter.

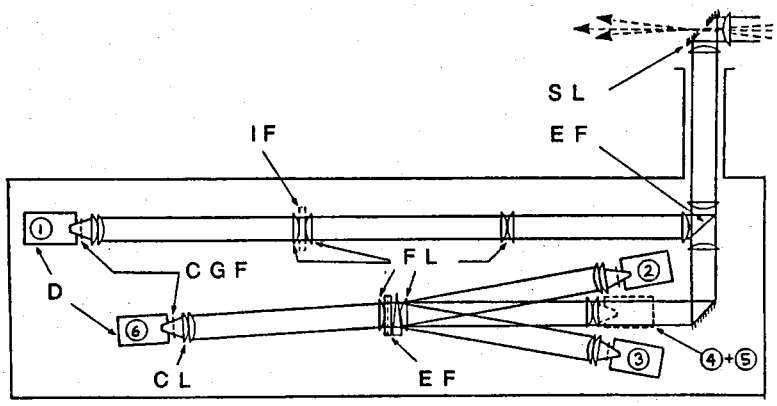

Fig. 9: Lay-out of the spectrometer. SL: slit mirror; EF: dielectric edge filter; FL: field lens; CL: condensor lens; CGF: coloured glass edge filter; D: detector; IF: interference bandpass filter (presently not inserted).

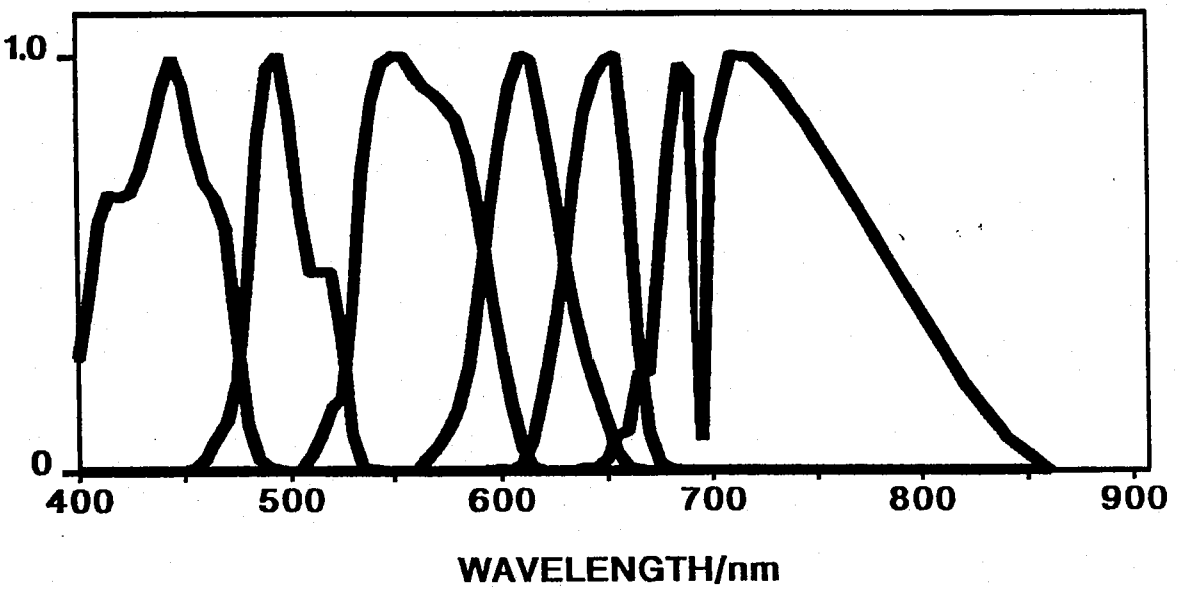

Fig.10: Spectral slit functions of the six channels (present set-up using the plane plate edge filters).

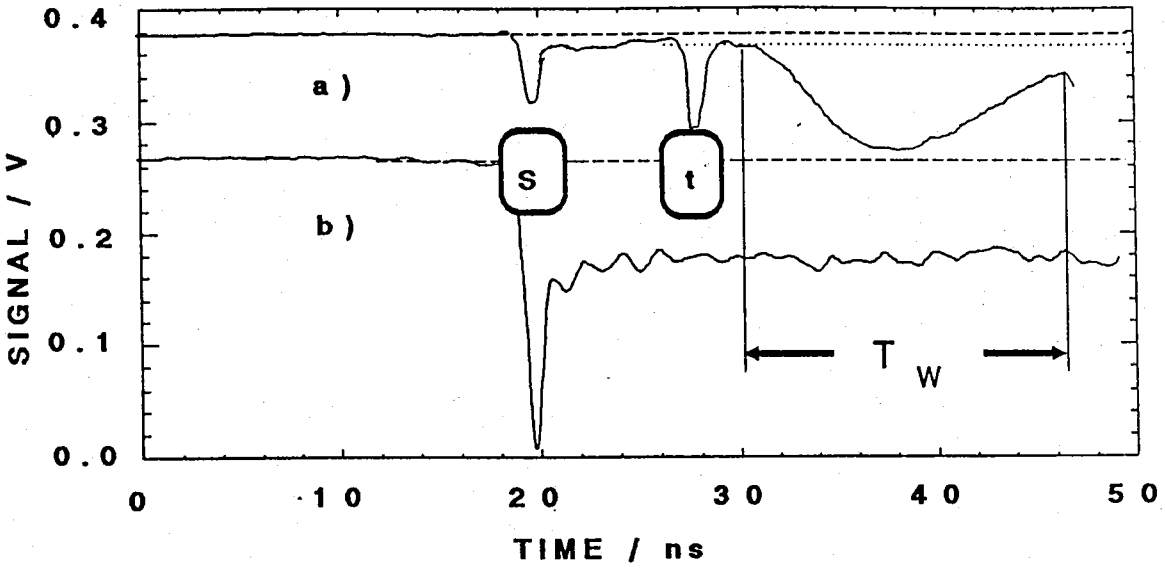

Fig.11: a) Raman scattering signal from air at p = 1 bar. Detector gain = 1.1 * 10^4. Neutral density filter ND 1.0. "t" indicates the time mark used for time correlation of the six signals. "T_w" is the time of measurement.

b) Flat top response of the gated detector during the time of measurement. Incandescent light source. Detector gain = 1 * 10^5. "S" idicates the "switch-on" pulse occurring during the voltage rise.

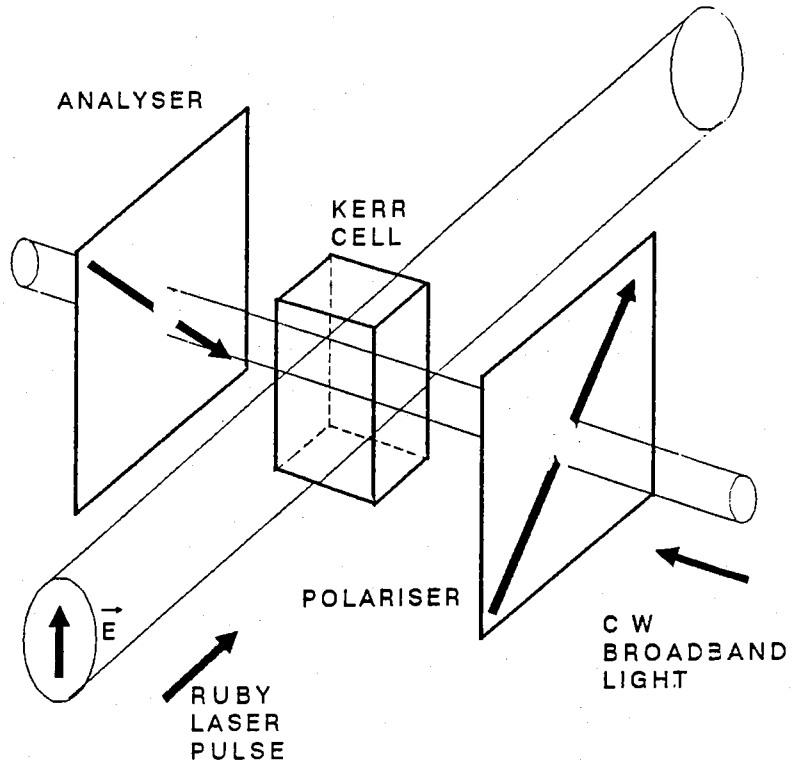

Fig.12: Set-up of the hf optical Kerr effect shutter experiment (schematic).

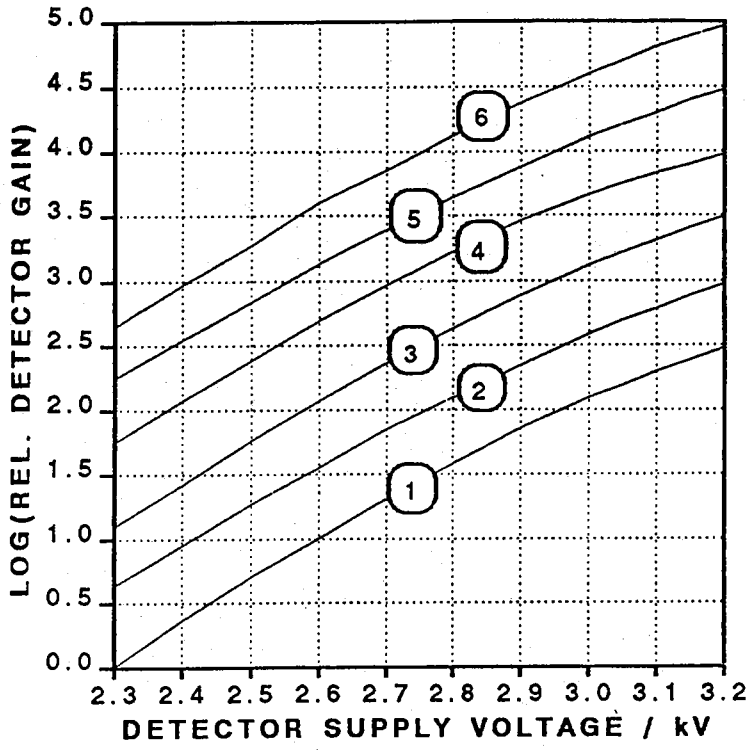

Fig.13: Relative gain of the detectors vs. detector supply voltage. Logarithmic plot. The curves are displaced vertically with respect to each other.

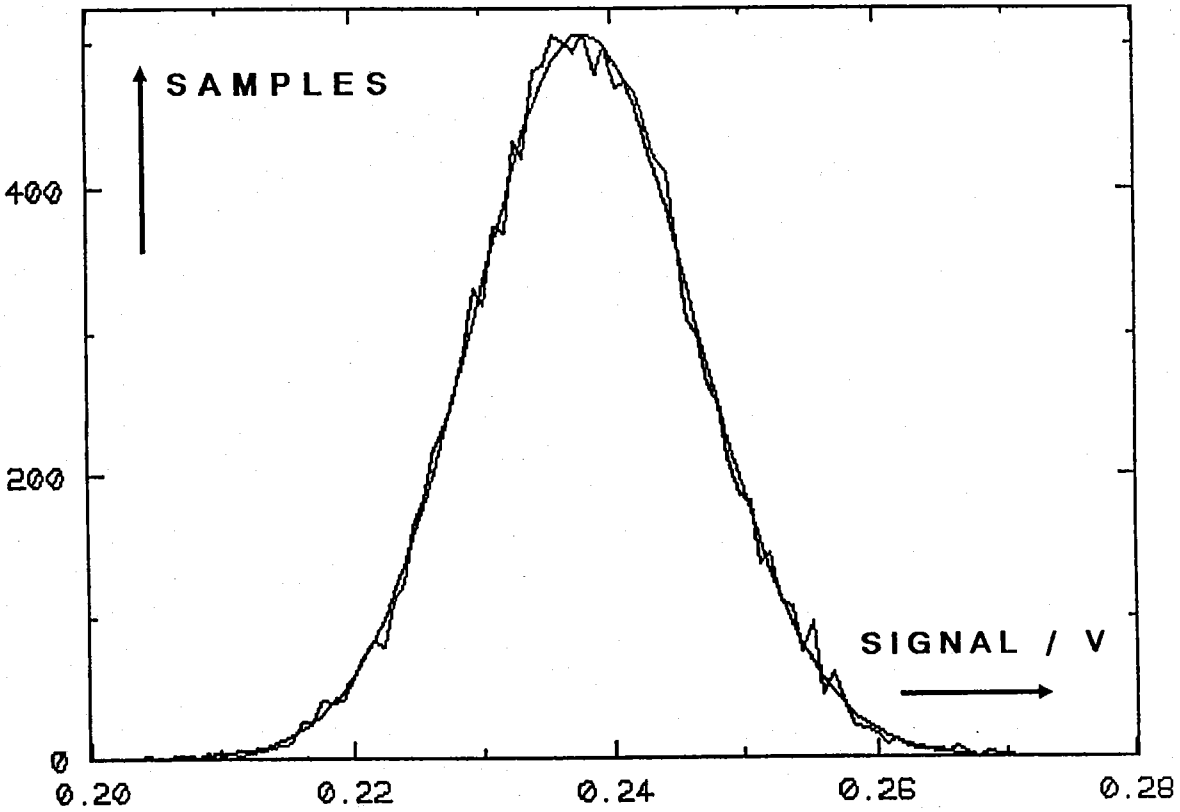

Fig.14: Histogram of signal fluctuations at DC illumination (spectral channel no. 1). The fitted curve is a best-fit Gaussian. Total number of samples 13965.

Fig 15(a)

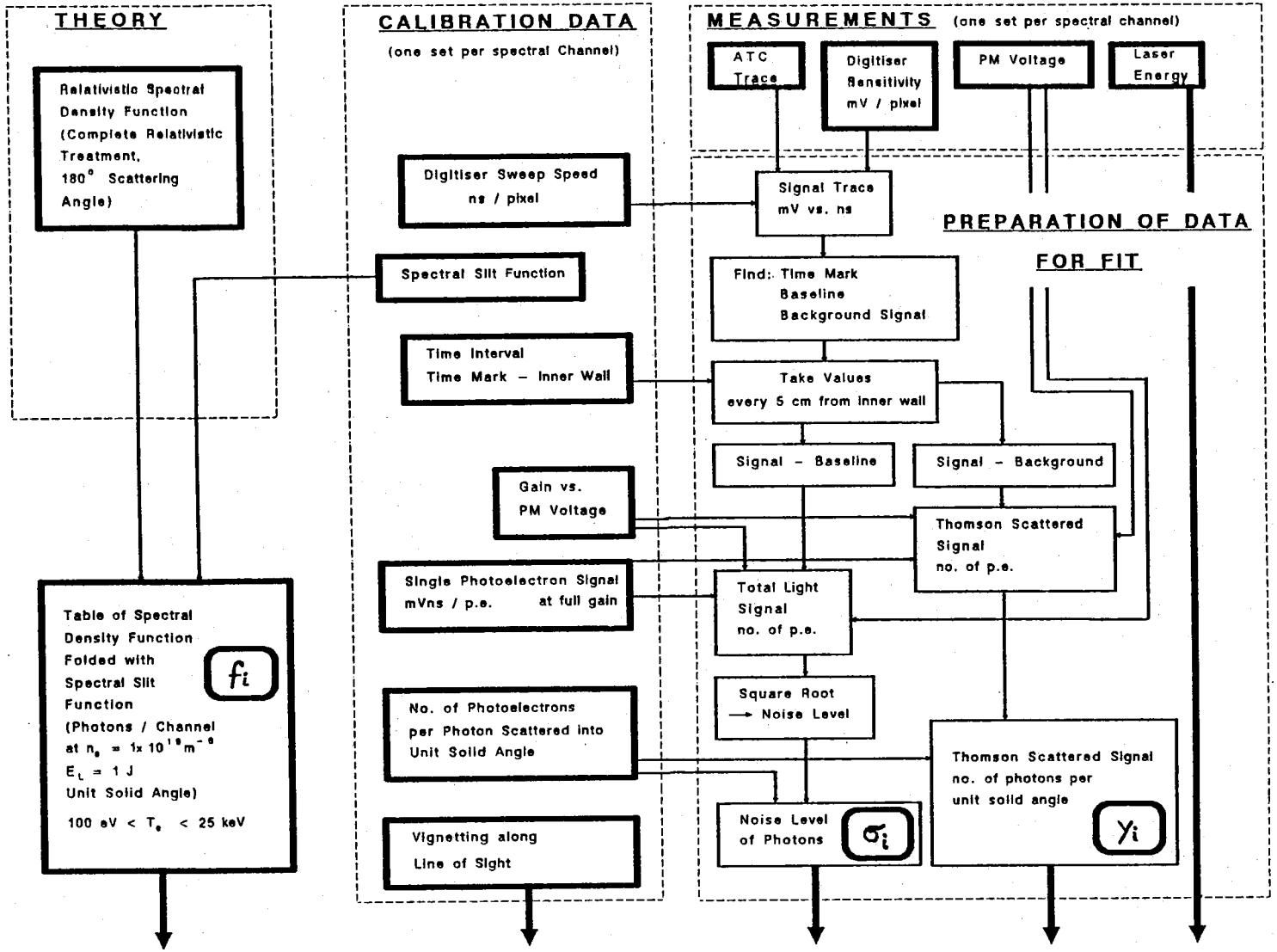
THEORY
Relativistic Spectral Density Function (Complete Relativistic Treatment, 180° Scattering Angle)
Table of Spectral Density Function Folded with Spectral Slit Function (Photons / Channel at $n_e = 1 \times 10^{19} m^{-3}$ $E_L = 1$ J Unit Solid Angle)
f_i
100 eV < T_e < 25 keV
CALIBRATION DATA
(one set per spectral Channel)
Digitiser Sweep Speed ns / pixel
Spectral Slit Function
Time Interval Time Mark – Inner Wall
Gain vs. PM Voltage
Single Photoelectron Signal mVns / p.e. at full gain
No. of Photoelectrons per Photon Scattered into Unit Solid Angle
Vignetting along Line of Sight
MEASUREMENTS (one set per spectral channel)
ATC Trace
Digitiser Sensitivity mV / pixel
PM Voltage
Laser Energy
PREPARATION OF DATA FOR FIT
Signal Trace mV vs. ns
Find: Time Mark Baseline Background Signal
Take Values every 5 cm from inner wall
Signal – Baseline
Signal – Background
Thomson Scattered Signal no. of p.e.
Total Light Signal no. of p.e.
Square Root → Noise Level
Noise Level of Photons
σ_i
Thomson Scattered Signal no. of photons per unit solid angle
y_i

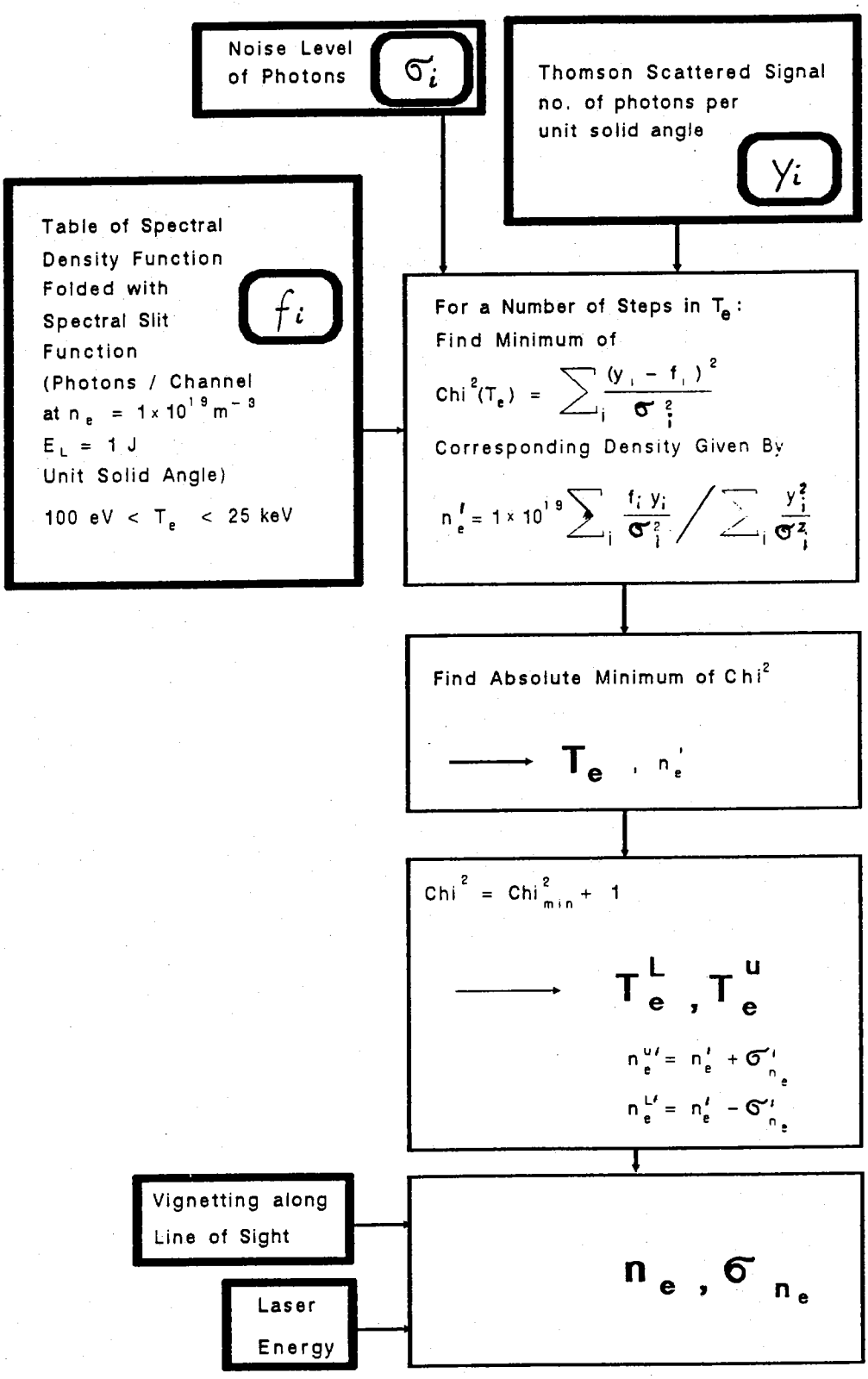

Fig.15: Flow chart of the numerical data evaluation.

Fig 15(b)

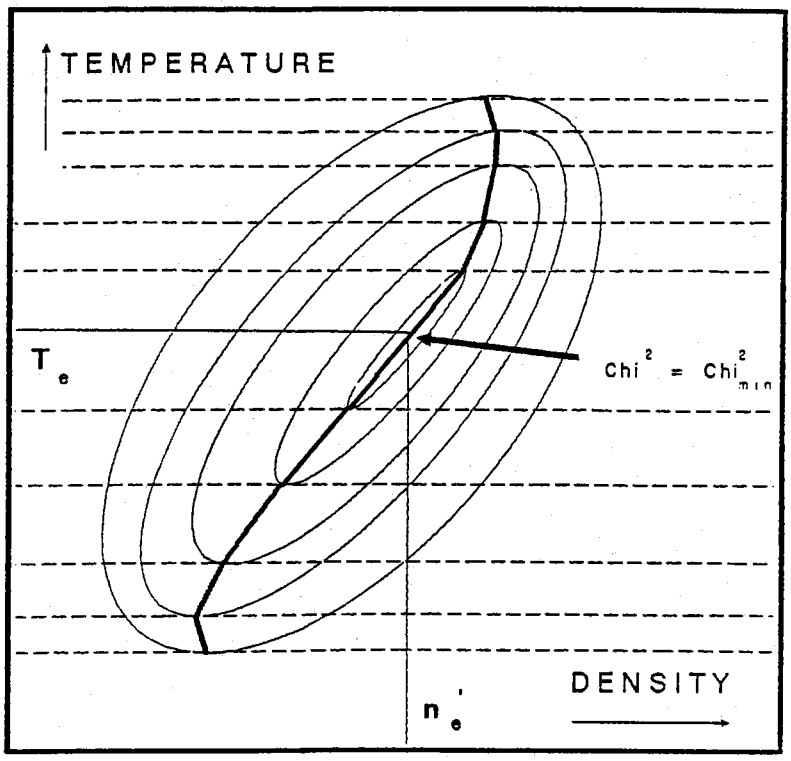

Fig.16: Best-fit procedure for finding the absolute minimum of Chi^2 in the T_e, n_e' plane (schematic). Closed lines are contour lines of Chi^2.

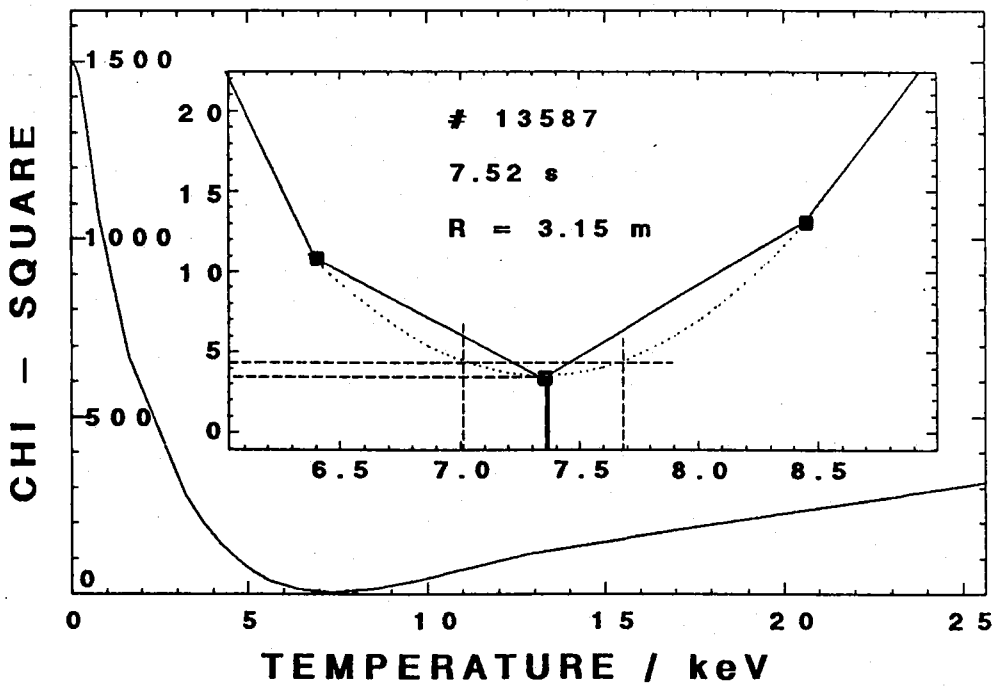

Fig.17: Chi^2 minimised with respect to density vs. electron temperature. The region of the minimum is shown with higher resolution in the insert. Dotted line: Parabola fitted through the three minimum Chi^2 values calculated. Evaluated values: T_e = 7.36 keV, $T_{e,min}$ = 7.0 keV, $T_{e,max}$ = 7.68 keV.

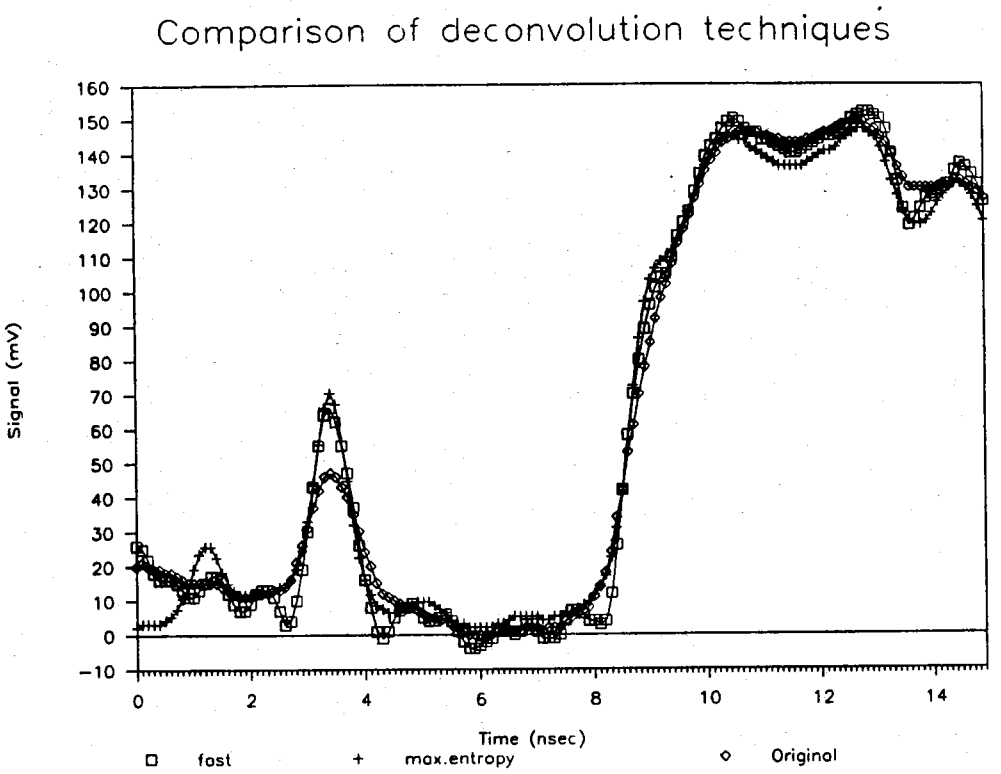

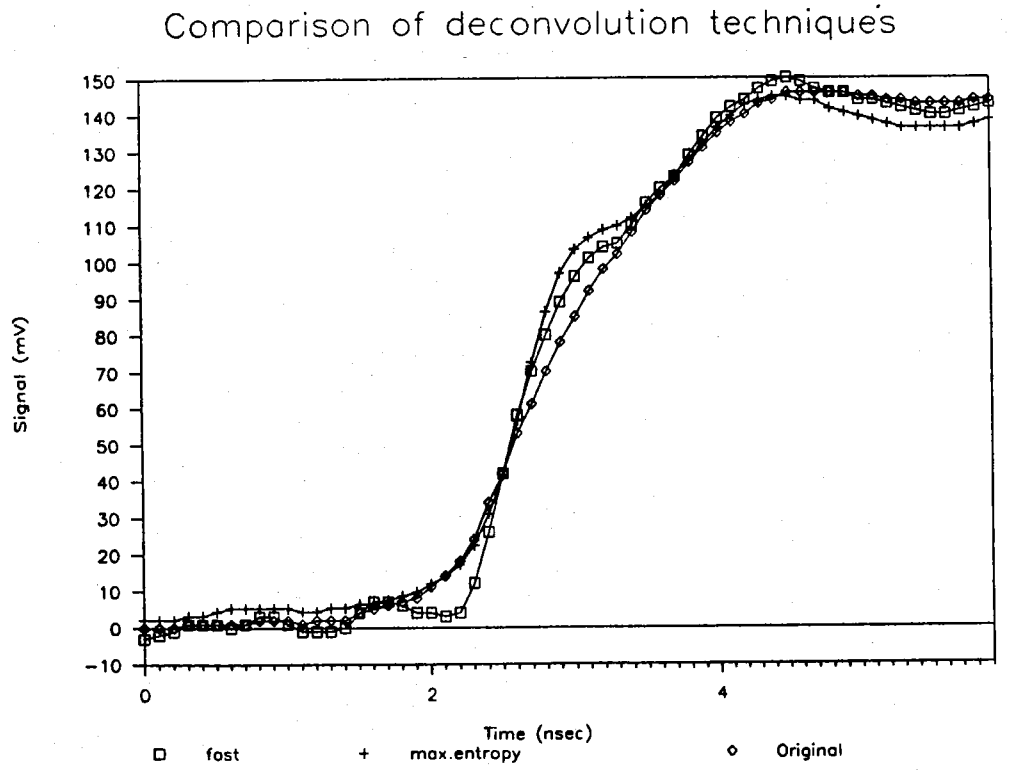

Fig.18: a) Raw signal of channel 1 (JET # 15886, t = 16sec) and signals deconvoluted by the maximum entropy method and by the fast numerical iteration method.
b) Same as a), rise of Thomson scattering signal expanded.

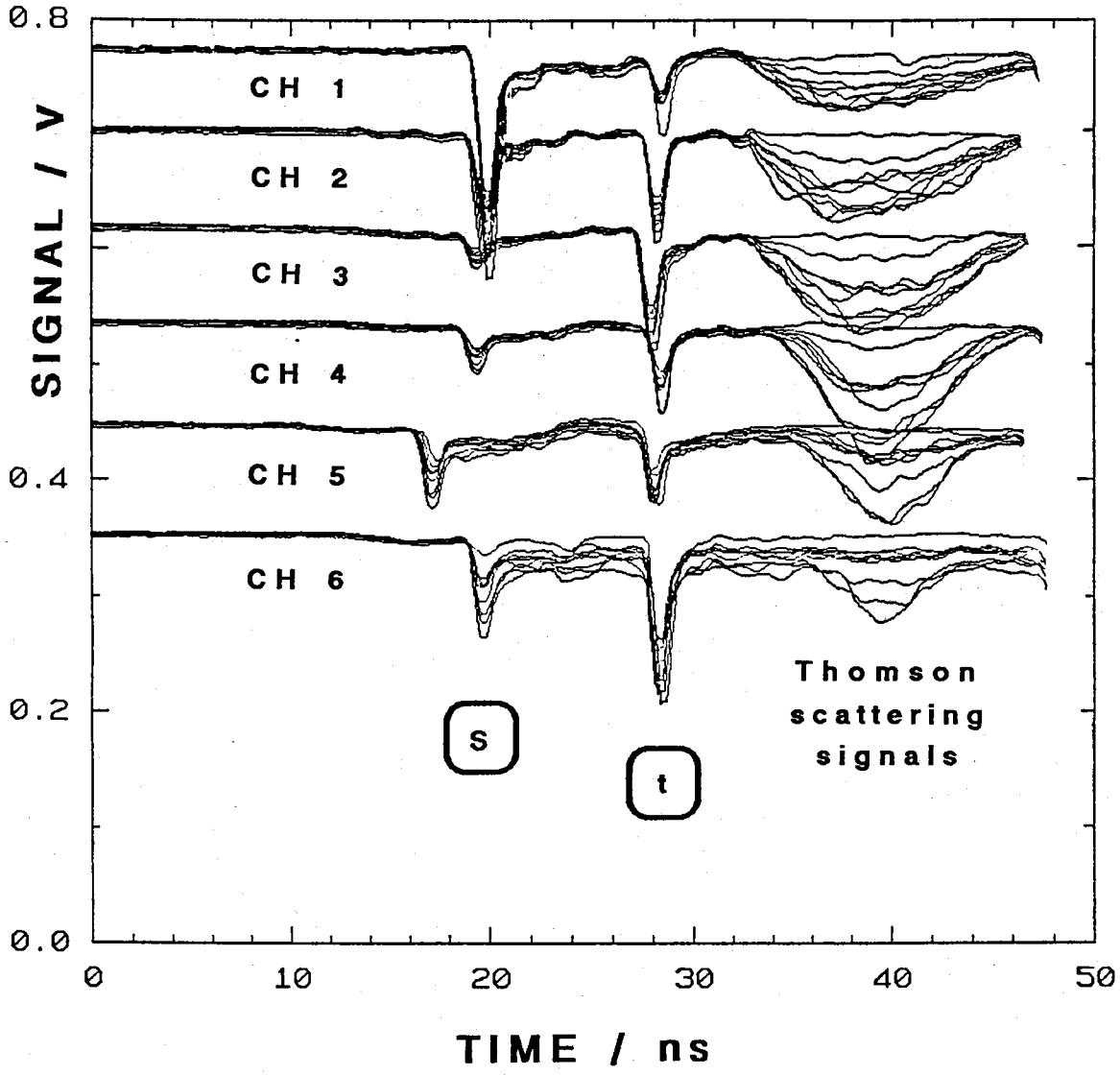

Fig.19: Signals from the 6 spectral channels vs. time. Signals are displaced vertically with respect to each other. Vertical sensitivity: 800 mV / full scale.

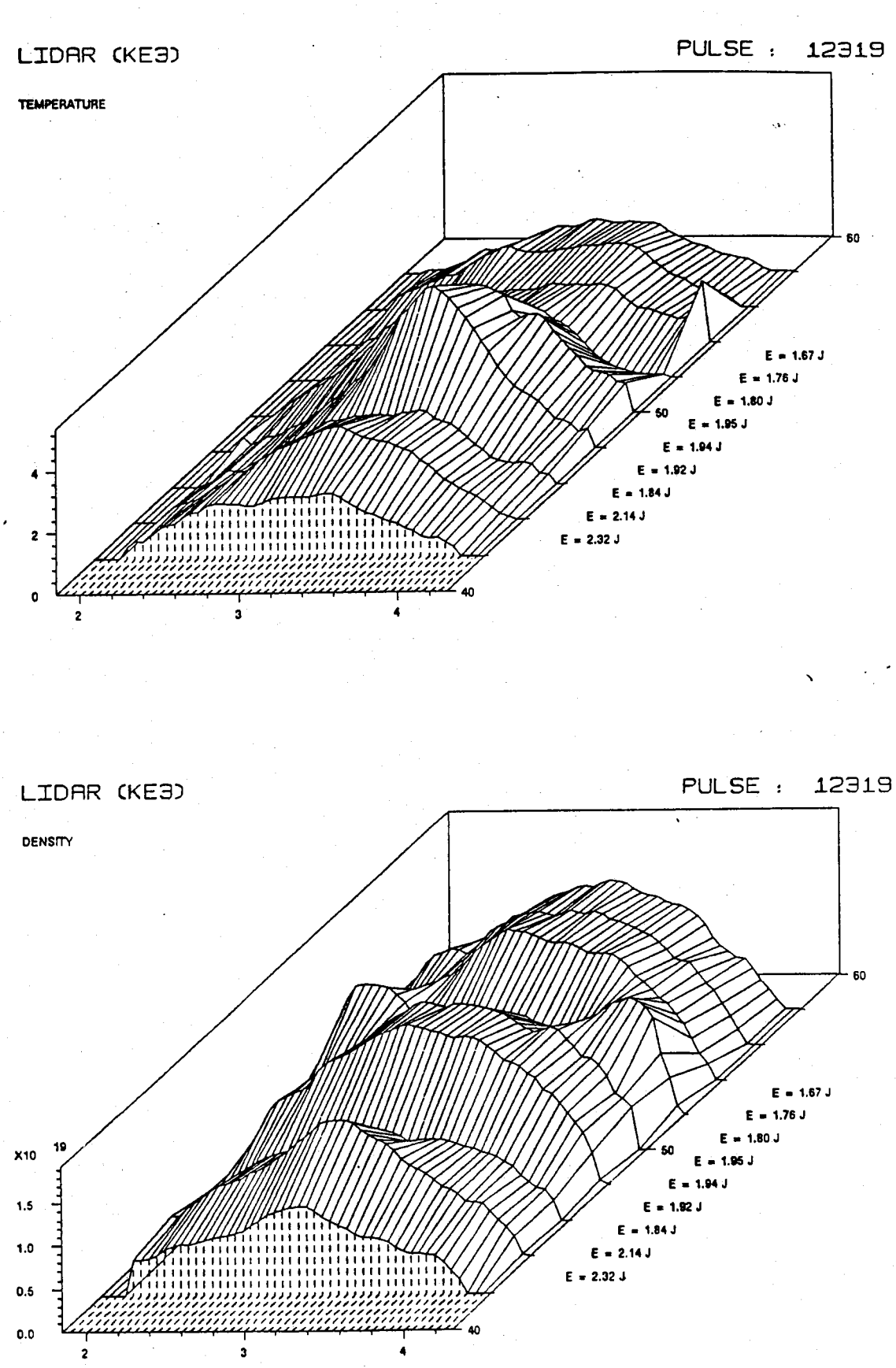

Fig.20: Three-dimensional plot of the temporal evolution of the radial profiles of T_e and n_e during a plasma discharge wth RF heating and pellet injection.

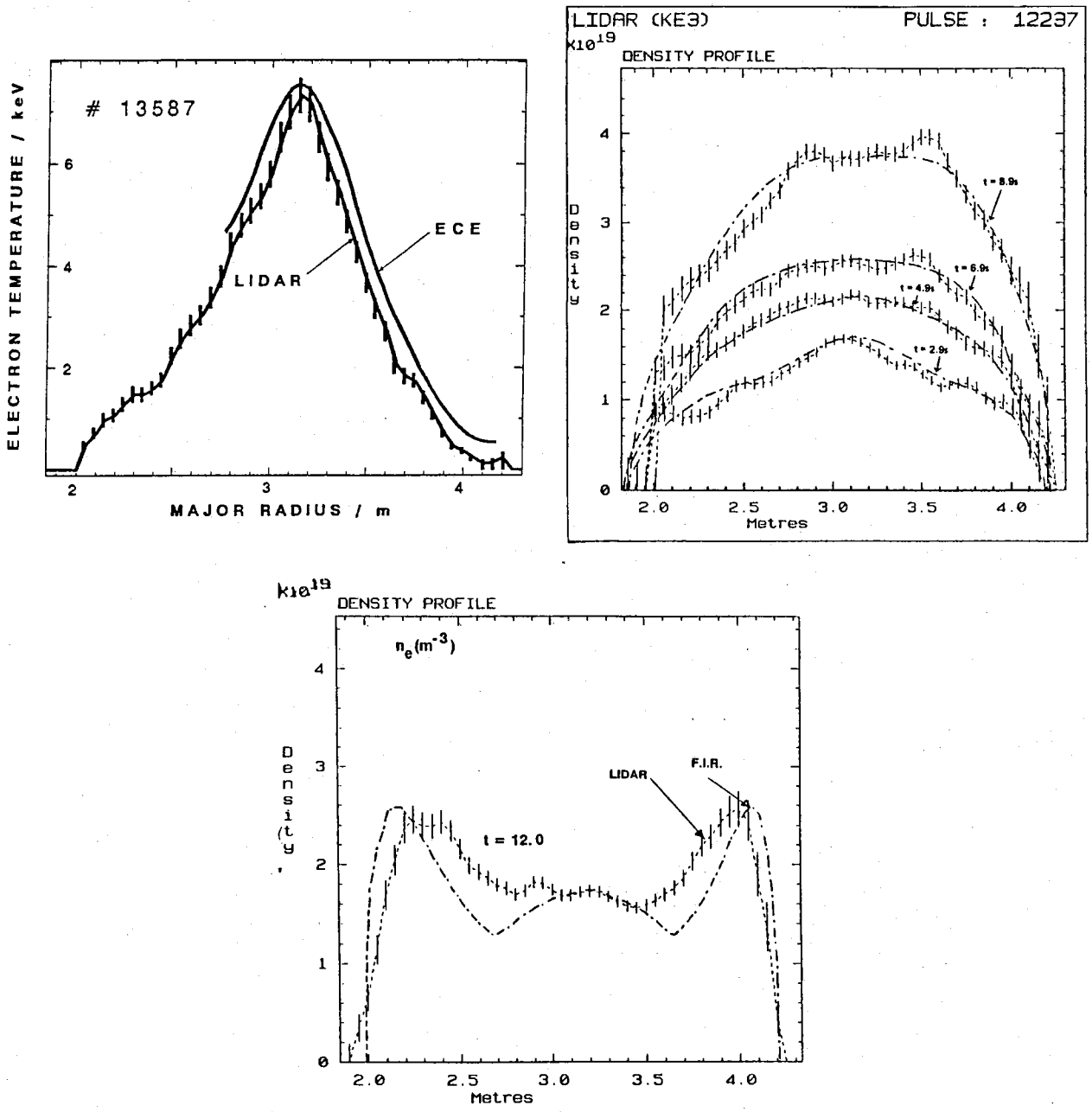

Fig.21: a) Comparison of a temperature profile obtained by the LIDAR Thomson scattering diagnostic during RF heating with the ECE results.
b) Comparison of density profiles from LIDAR with density profiles obtained from the FIR interferometer during an Ohmic discharge.
c) Comparison of density profiles during pellet injection.

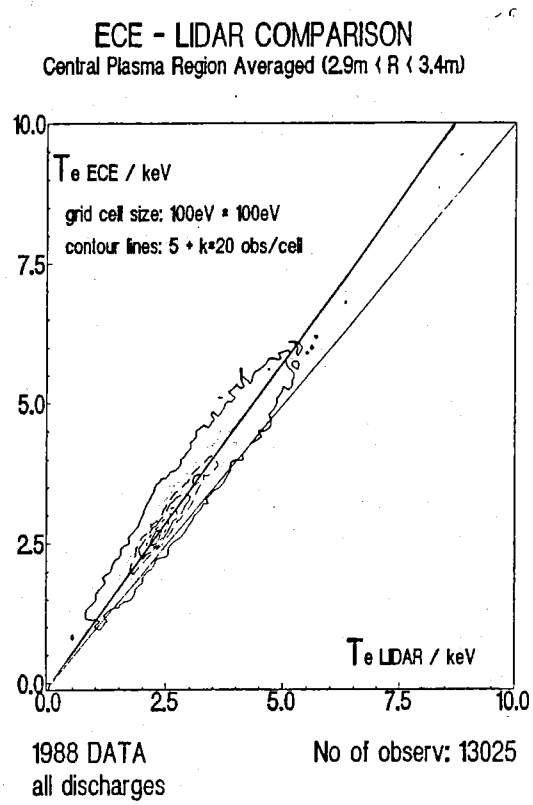

Fig.22: Te(LIDAR) vs. T_e(ECE). Temperature values are averaged over the central plasma region.

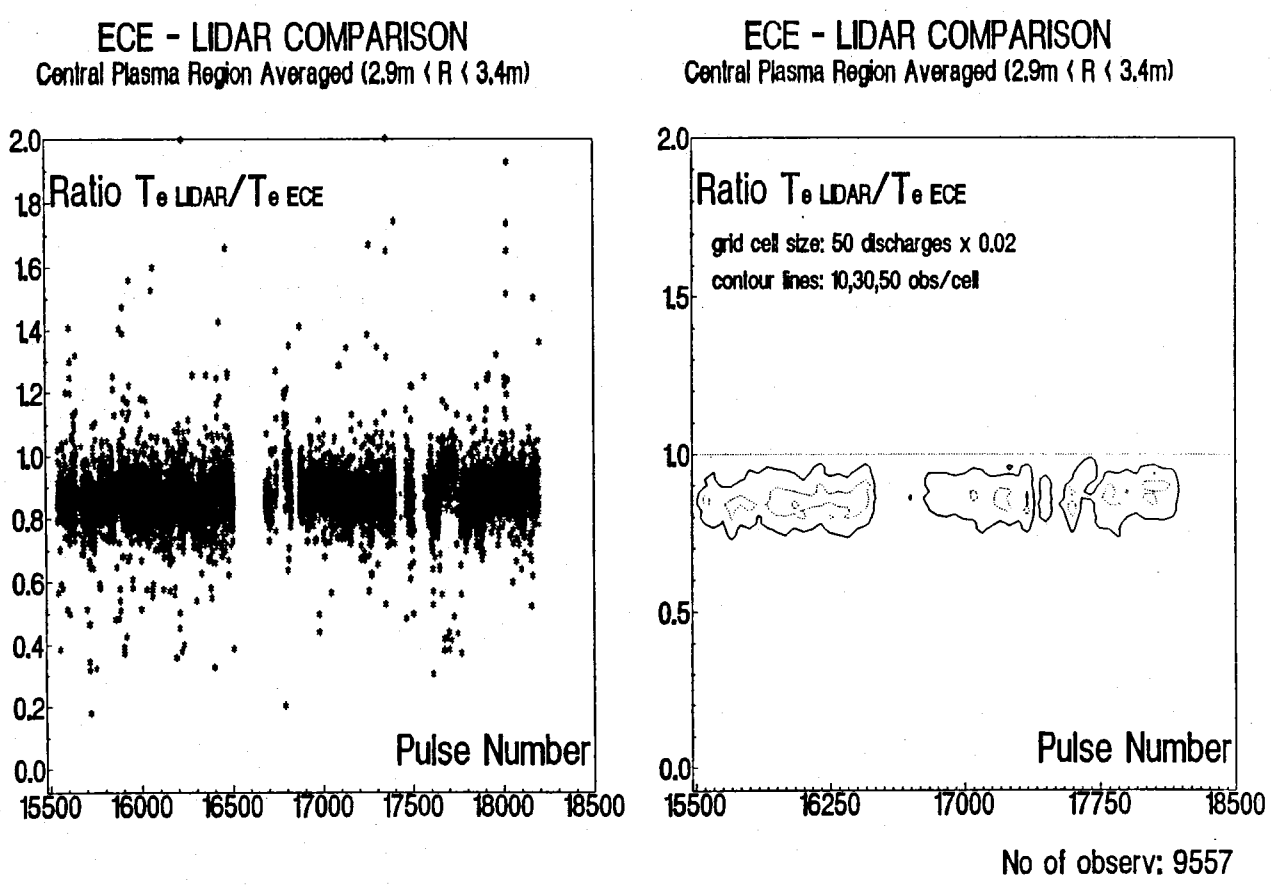

Fig.23: T_e(LIDAR)/T_e(ECE) vs. JET pulse number. Temperature values are averaged over the central plasma region.

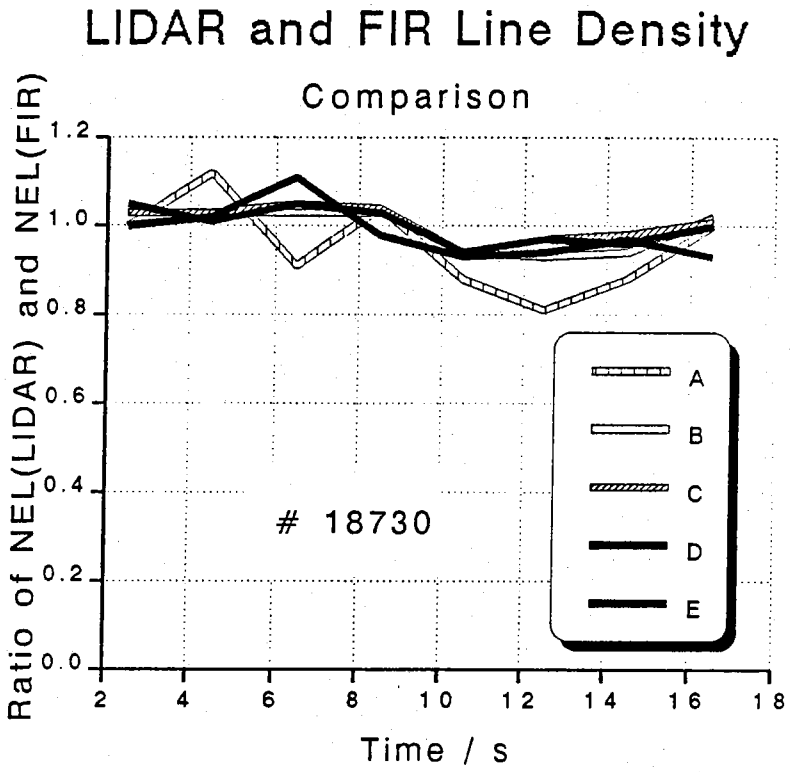

Fig.24: Temporal evolution of the ratios of the line integrated electron densities from LIDAR data and those from direct FIR interferometer measurements. A - E: Vertical FIR interferometer channels located at R = 2.17, 2.70, 3.02, 3.34, 3.75 m.

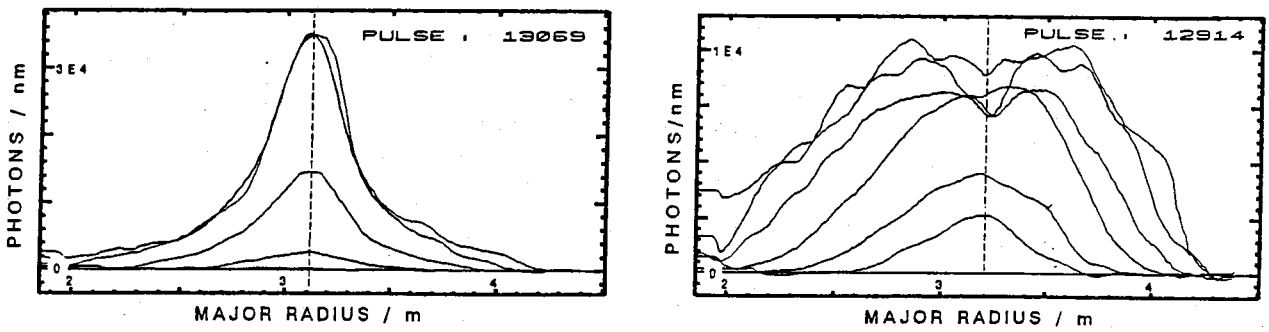

Fig.25: a) Processed data of scattering signals for plasma with pellet injection (time converted to major radius, signal amplitude converted to collected scattered photons/nm wavelength interval). Completely automatic data processing.
b) Processed data of scattering signals for RF-heated plasma.

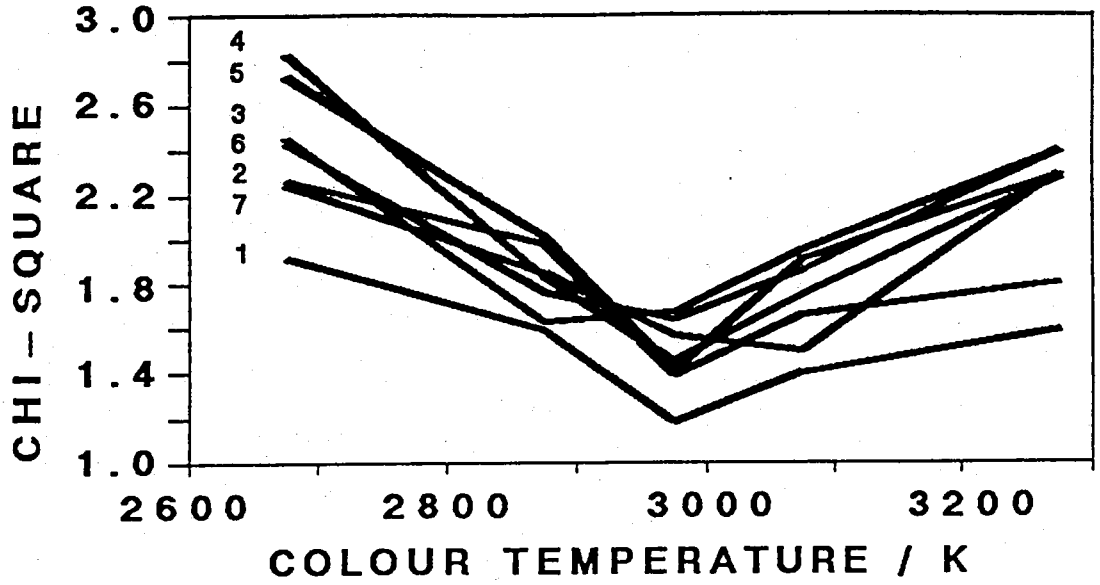

Fig.26: Chi² test applied to the colour temperature of the black body standard lamp used for calibration. Chi² vs. assumed colour temperature. 1-7: Results from fits in the temperature ranges 2.0-2.4, 2.4-2.8, 2.8-3.2, 3.2-3.6, 3.6-4.0, 4.0-4.4 and 4.4-4.8 keV. 60 measurements per interval.

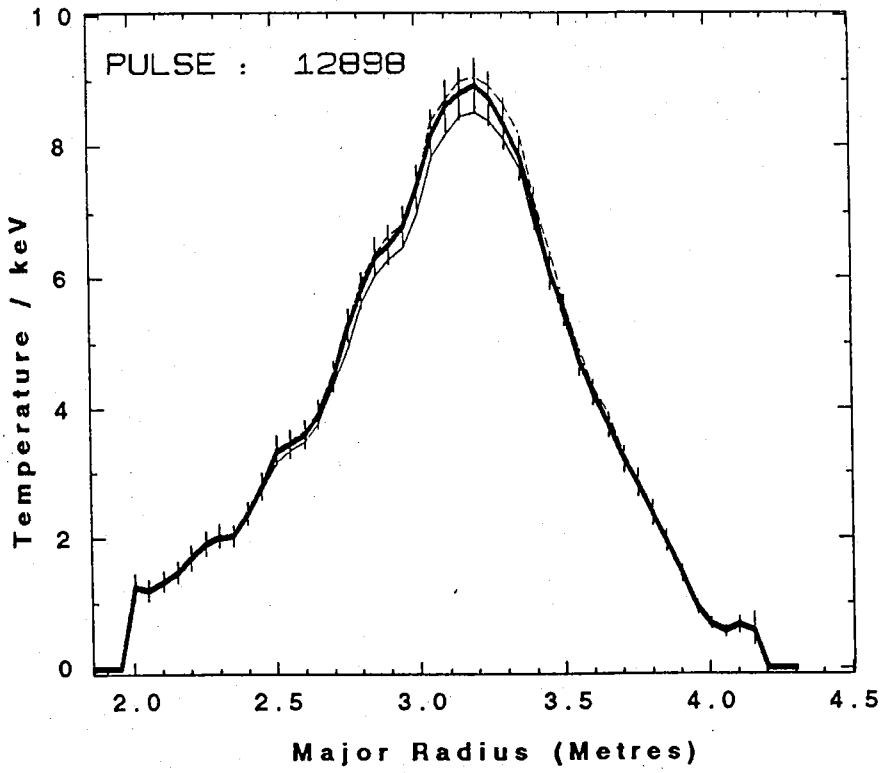

Fig.27: Bold solid line: Electron temperature profile and error bars (thin lines) from fit for T = 2973 K (JET # 12898, t=11.8 s, RF heated plasma, "monster" sawtooth).
Thin solid line: Fit for T = 2923 K. No error bars plotted.
Thin broken line: Fit for T = 3023 K. No error bars plotted.